Understanding the driving forces of the phase transition in SnxTi1-xO2 via the effective site energy model

F. Berthier, R. Tétot, B. Legrand

Understanding the phase transition driving forces of $Sn_xTi_{1-x}O_2$ via the Effective Site Energy model

F. Berthier[1], R. Tétot[1], B. Legrand[2]

[1] Université Paris-Saclay, CNRS, Institut de Chimie Moléculaire et des Matériaux d'Orsay, 91405, Orsay, France.

[2] Université Paris-Saclay, CEA, Service de Recherche en Corrosion et Comportement des Matériaux, SRMP, 91191, Gif-sur-Yvette, France.

Abstract

For the first time, an approach coupling the variable charge model per bond based on a tight-binding approach within the second moment approximation (SMTB-QB) and the Effective Site Energy (ESE) is used to obtain the phase diagram of a mixed oxyde. SMTB-QB allows one to calculate the site energies of all atoms in random solid solution for the $SnTiO_2$ mixed oxide. These energies are analyzed within the ESE model as a function both of the local environment (number of Sn nearest neighbors) and of the nominal concentration. The almost symmetrical miscibility gap is well reproduced by rigid lattice ESE Monte Carlo simulations. The ESE model shows that the apparent symmetry of the phase diagram actually comes from two highly asymmetrical thermodynamic forces. The local effect that induces a homoatomic short range order (SRO) dominates when Sn is the minority element, while the non-local effect that does not induce SRO dominates when Sn is the majority element. This result demonstrates that the ESE model's ability to analyze the driving forces that govern phase diagrams, which has been widely demonstrated for bimetallic alloys, also extends to mixed oxides.

I. INTRODUCTION

Mixed metal oxides have a wide range of applications in the fields of electronics, energy storage, gas sensor, catalysts for pharmaceuticals or batteries. Their properties may be significantly modified by combining two or more different types of metal cation. Studies show that the structural and local environment of cations can also play a major role in disordered mixed oxides [1–3], and that cationic disorder is not always detrimental to material performance [1]. Understanding phase diagrams is therefore essential for precise control of the structure and chemical composition of these materials. In addition, to control the mechanical, chemical and functional properties of materials, it is essential to understand the relative importance of the local order driven by local chemical interactions, generally known as the chemical effect and hereafter referred to as the local effect, and the effect induced by the nominal composition, referred to as the non-local effect. This effect could include elastic effects due to the different atomic radii of the cations, electronic effects or other effects such as magnetic effects. Controlling the local and non-local effects opens the way to the generation of new materials with both high mechanical stability and high chemical reactivity.

Atomistic modelling can be a powerful tool in order to compute thermodynamic properties of mixed oxides and equilibrium phase diagrams. Different approaches are used such as phenomenological models to describe the energetics of mixing and phase stability in solid solutions [4–8], rigid-lattice Monte Carlo simulations using an energetic model based on pairwise interactions [9–11] or more interactions (pairs, triplets…) issued from the cluster expansion (CE) method [12,13], or Monte Carlo simulations based on semi-empirical interatomic potentials [14–21]. The separation of non-local and local effects, and their relative importance, remains tricky from both experimental [1,2] and theoretical [6,12,22] points of view.

We consider in this work an alternative method to the CE [23–27], the effective site energy (ESE) approach which was originally developed for A_cB_{1-c} bimetallic alloys [28–30]. While CE is based on the energy calculation of a large number of ordered structures, the ESE method involves determining the energies of atoms in random solid solutions (rss). These energies take into account relaxation of local atomic position and the volume optimization. Local relaxations of ordered phases are much weaker than in rss, which is why the ESE method is

probably more effective than the CE method for taking local relaxations into account. Furthermore, unlike the CE, the calculation of the ESE converges very quickly.

Site energies are calculated using atomistic simulations based on interatomic potentials at $T = 0$ K. The site energies $E_I^p(c)$ $(I = A, B)$ are averaged as a function of the chemical composition of their local surrounding p, and of the nominal concentration c. The local composition p was defined as the number of A atoms in the nearest-neighboring shell. We have shown that this limitation to nearest neighbors is sufficient in bimetallic alloys. For metals, site energies were calculated using semi-empirical interatomic potentials derived from the second-moment approximation of the tight-binding scheme (SMA-TB) [31]. The development of a mean-field model from the ESEs leads to an analytical expression of the enthalpy of mixing and the local and non-local contributions. The local contribution is related to the effective pair interactions (EPIs) that drive the short-range order (SRO). The non-local contribution does not lead to local order. As the attractive energy derived from SMA-TB, considers only the width of the *d*-band density of states, and not all its details, it makes possible to exclude any energy dependence on concentration other than the elastic contribution. In absence of other effects, such as magnetism or electronic effects, the dependency of the ESE with the nominal concentration is mainly linked to the elastic effects due to the change in lattice parameter of the pure binary metals. That's why for metals, the local and non-local contributions are also named chemical and elastic or size effects. This decomposition enables both effects to be quantified over the entire concentration range. Hence, the ESE model is a useful theoretical tool to separate the effects of the local (chemical) environment from those of the global (elastic) composition.

In this article, we focus on a binary oxide, SnO_2–TiO_2, which has been the subject of numerous experimental and theoretical studies for its gas detection and electrical properties [11,32–38]. The $SnTiO_2$ phase diagram exhibits a large miscibility gap [11,15,39–42]. Liu *et al.* calculated a critical demixing/disordering temperature of around 2000 K [11]. Experimentally, the critical temperature is slightly lower, close to 1800 K [41,42]**.** This value is consistent with other experimental studies.

The aim of this article is therefore to extend the ESE method to mixed oxides by applying it to the $SnTiO_2$ system. For mixed oxides, the question arises as to whether the local environment can be limited to the nearest neighboring cations in this iono-covalent system where long-range interactions (coulombic) take place.

We consider here a new version of the so-called SMTB-Q model (Second-Moment Tight-Binding QEq) [43,44], the SMTB-QB model (B for bond) based on a quantum description of oxides proposed by Goniakowski and Noguera [45]. From these interatomic potentials we perform Monte Carlo (MC) simulations with atomic position relaxations, at temperatures close to 0 K, to determine the average site energies $E_I^p(c)$ $(I = Sn, Ti, O)$ of rss as a function of local chemical composition p (number of Sn atoms in the nearest neighboring of the considering atom) and nominal concentration c.

We define a Hamiltonian from site energies that is introduced in a mean-field formalism (ESE-MFA) and in rigid lattice Monte Carlo simulations (ESE-MC) to get isotherms and the phase diagram. The ESE-MFA provides an analytical expression for permutation and mixing enthalpies, a decomposition into local and global contributions. The ESE-MC simulations also provide local order.

The paper is organized as follows. In Section II.A we give a short presentation of the system and we present the energetic models. We introduce the SMTB-QB interatomic potentials (sec. II.B) and the ESE model (sec. II.C). Then we check the validity of the ESE model (sec. II.D). In Section III we detail the ESE mean field approximation (ESE-MFA), we define by matching with the Ising model the local and the non-local contributions to the permutation and mixing enthalpies (sec. III.B) and we present the results (sec. III.C). Thereafter, ESE-MFA isotherms and phase diagram are described (sec. III.D). Section IV is devoted to the results of ESE-MC simulations compared with the ESE-MFA. Isotherms and SRO issued from MC simulations are presented. Finally, in Section V we conclude and discuss possible outlooks.

II. SYSTEM AND ENERGETIC MODELS

A. System

SnO_2 and TiO_2 crystallize in the rutile structure illustrated in FIG. 1(a). This structure belongs to the *P4₂/mnm* tetragonal space group. The unit cell contains two cations (located in the corners and in the center of the cell) and four oxygen anions. Each cation is octahedrally coordinated to six oxygen ions. The coordination number is therefore $Z_C = 6$ for cations and $Z_O = 3$ for oxygen.

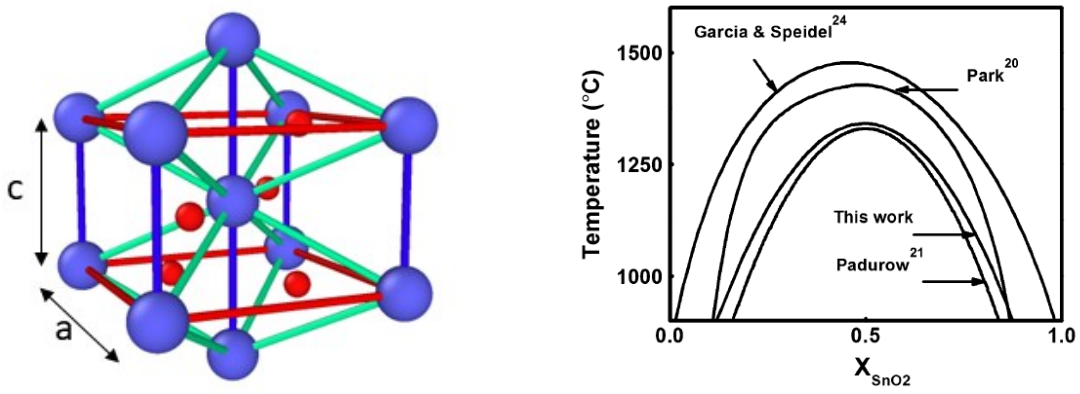

(a) (b)

FIG. 1. (a) Rutile structure: cations are in blue and oxygen in red. Bonds between cations are colored as a function of their lengths. A cation (see the central atom) has two first neighbors at d_s (blue bonds) and eight first neighbors at d_l (green bonds). Red bonds are longer. (b) $SnTiO_2$ temperature-composition phase diagram issued from [42] (references cited on the figure are: Padurow [39], Garcia and Speidel [40], Park *et al*. [41]).

The Sn(Ti)O_2 octahedron is distorted and slightly elongated along the <110> direction. The unit cell is defined with two lattice constants *a* and *c* and an internal parameter *u* which fixes the relative position between cations and oxygen. A cation has $Z = 10$ nearest neighbor cations with two short distances (d_s) and eight long distances (d_l), see FIG. 1(a). The different data for TiO_2 and SnO_2 are resumed in TABLE 1.

	TiO_2	SnO_2
a (Å)	4.594	4.74
c (Å)	2.959	3.19
u	0.305	0.3069
dl (Å)	3.57	3.71
ds (Å)	2.96	3.19

TABLE 1: Lattice constants, internal parameter and cation-cation distances in TiO_2 and SnO_2 structures. Data are from [46] for TiO_2 and from [47,48] for SnO_2.

FIG. 1(b) shows the temperature-composition phase diagram of the SnO_2-TiO_2 mixed-oxide system. The phase diagram presents a large miscibility gap reflecting a phase separation under a critical temperature of about 1400 °C at $X_{SnO_2} = 0.5$.

B. SMTB-QB interatomic potentials

We use here a new version of the so-called variable-charge SMTB-Q model [43,44,49], named SMTB-QB model with B for bond. In the SMTB-Q model, the equilibrium charges in a given configuration of the ions in the simulation box are computed using the QEq scheme by Rappé and Goddard [50]. These charges are the ones which minimizes the energy of the box with the constrain of the *global electric neutrality*. This approach, which works well for pure oxides, cannot address rigorously multi-cation disordered solutions as studied here. To overcome the problem, the SMTB-QB model consider the charge transfer between oxygen and cations locally (by bond) instead of globally, as developed in the Bond Electron Transfer Model (BETM) by Noguera *et al*. [51]. As a result, this model is more constrained than the previous one since now it ensures *local electrical neutrality*. Moreover, this new version of the model allows the study of charged defects and the evaluation of the electronic gap in an oxide [52].

In both the SMTB-Q and SMTB-QB models, the cohesive energy of a pure oxide (TiO_2 or SnO_2), E_{coh}, is the sum of 4 terms:

$$E_{coh} = E_{ion} + E_{coul} + E_{rep} + E_{cov} \quad (1)$$

$E_{ion}, E_{coul}, E_{rep}$ are exactly the same in the two models and are described elsewhere [43,44,49]. Let's just remember that:

$$E_{ion} = \sum_A \left(E_A^0 + \chi_A^0 Q_A + \frac{1}{2} J_{AA}^0 Q_A^2 \right) \quad (2)$$

where Q_A is the charge of the atom *A*. χ_A^0, J_{AA}^0 and E_A^0 are respectively the electronegativity, the hardness and the energy of neutral atom *A*. E_A^0 is taken as zero for all species.

$$E_{coul} = \sum_A \sum_{B<A} Q_A Q_B J_{AB} \quad (3)$$

where J_{AB} is the Coulomb integral between two *ns*-type Slater orbital which represents the spherical charge distribution of atoms *A* and *B* respectively: $\Phi_n^{Slat} = N_n r^{n-1} \exp\left[-\frac{(2n+1)r}{4R_A^{eff}}\right]$. N_n is the normalization constant, n is the quantum number for the outer valence orbital ($n = 3$ for Ti, 5 for Sn and 2 for O) and R_A^{eff} is the effective radius of the atom *A* which is an adjustable parameter. J_{AB} is equal to the classical $1/r$ Coulomb interaction when $r \gtrapprox 5$Å.

$$E_{rep}(M-O) = \sum_{i=M,O} \sum_{j=O,M} A_{M-O} \exp\left[-p\left(\frac{r_{ij}}{r_0} - 1\right)\right] \quad (4a)$$

$$E_{rep}(O-O) = \sum_{O}\sum_{O} A_{O-O} \exp\left[-\frac{r_{OO}}{\rho}\right] \quad (4b)$$

These terms (Eqs. 4(a,b)) reflect the short-range Pauli repulsion. Short-range repulsion between two cations may be generally neglected because of their great first neighbor distance (≥ 3. Å) and the high electrostatic repulsion between them. For each pure oxide (TiO_2 or SnO_2), A_{M-O} and p, are adjustable parameters and r_0 is the distance between the first Ti(Sn)-O neighbor at equilibrium ($r_0 = 1.95$ and 2.054 Å in TiO_2 and SnO_2 respectively). The parameters relative to oxygen (A_{O-O}, ρ) are the same for each oxide and have been determined in previous studies [44].

The difference between SMTB-Q and SMTB-QB models lies in the covalent term E_{cov}. In both cases, E_{cov} derives from the tight-binding approach by Noguera and co-workers [45,53] which accounts for the mixed iono-covalent character of the oxygen–cation bond in an insulating oxide. E_{cov} is a cohesive band term which is a function of both electron hopping integrals, ξ_{ij}, resulting from the hybridization between cations C_j and oxygen ions O_i orbitals, and the ionic charges Q_j and Q_i: $E_{cov} = f(\xi_{ij}, Q_j, Q_i)$. As $E_{rep}(M-O)$, ξ_{ij} is an exponentially decreasing function of distance:

$$\xi_{ij} = \xi_0 exp\left[-q\left(\frac{r_{ij}}{r_0} - 1\right)\right] \quad (5)$$

where ξ_0 and q are adjustable parameters.

We consider here only the hybridization between outer Ti *3d* and *4s* orbitals (with degeneracy $d_{Ti} = 6$), Sn *5p* and *5s* orbitals (with degeneracy $d_{Sn} = 4$) respectively and *2p* orbitals of O (with degeneracy $d_O = 3$). From the work of Noguera and co-workers [51], the electron back-transfer per bond between an oxygen anion and a cation (Ti or Sn), due to orbital hybridization can be expressed in a simplified form as:

$$\Delta_{O_i,C_j} = n_{ij}^0 \times T_j, \quad (6)$$

with $n_{ij}^0 = min\left(\frac{Z_C}{Z_O} d_O, d_C\right) \times \frac{\xi_{ij}^2}{\sum_{i\in j} \xi_{ij}^2}$ and $T_j = \left(1 - \frac{x_j}{\Delta_j}\right)$.

n_{ij}^0 represents the bond connectivity between O_i and C_j ions in the pure oxide. $Z_O = 3$ and $Z_C = 6$ in TiO_2 and SnO_2. The sum $\sum_{i\in j} \xi_{ij}^2$ extends to the neighboring oxygen O_i of cation C_j (symbol ∈) up to the second-moment cut off radius (~ 6 Å). The term T_j can be seen as the

electron transfer itself. In this term $x_j = \epsilon_{C_j} - \langle \epsilon_{O_i} \rangle_j$ is the difference between atomic energies of outer Ti(Sn) orbitals and O *2p* respectively (in fact $\langle \epsilon_{O_i} \rangle_j$ is the average value of all ϵ_{O_i} in the box (see [51] for details)).

$\Delta_j = \sqrt{x_j^2 + y_j^2}$ is the local HOMO-LUMO gap, which contains an ionic part x_j^2 and a covalent part $y_j^2 = 4 \sum_{i \in j} Z_{O_i} \xi_{ij}^2$. The total electron transfer from ions O_i to a cation C_j is:

$\delta Q_{C_j} = \sum_{i \in j} \Delta_{O_i, C_j} = n_j^0 T_j$ where: $n_j^0 = \sum_{i \in j} n_{ij}^0 = min\left(\frac{Z_C}{Z_O} d_O, d_C\right)$ (equals to 6 in a TiO_2 crystal and 4 in a SnO_2 crystal). The total electron back-transfer from an oxygen O_i is:

$\delta Q_{A_i} = \sum_{j \in i} \Delta_{O_i, C_j} = \sum_{j \in i} n_{i,j}^0 \times T_j$ (now T_j cannot be removed from the sum).

Consequently, the charge of a cation an oxygen is respectively:

$$Q_j = Q_{C_j}^F - n_j^0 T_j \text{ and } Q_i = Q_O^F + \sum_{j \in i} n_{ij}^0 T_j \quad (7)$$

where $Q_{C_j}^F$ and Q_O^F are the formal charge of a cation and of oxygen ion respectively ($+4$ for Ti and Sn and -2 for O).

The tight-binding approach leads to the expression of the total covalent energy $E_{cov} = \sum_j E_{cov}^j$, where E_{cov}^j is the covalent energy related to a cation C_j:

$$E_{cov}^j = -n_j^0 \frac{y_j^2}{\Delta_j}. \quad (8)$$

Eliminate x_j between E_{cov}^j and δQ_{C_j} leads to: $E_{cov}^j = -y_j \sqrt{\delta Q_{C_j}\left(2n_j^0 - \delta Q_{C_j}\right)}$.

Now, for a given configuration of the atoms in the simulation box, and whatever the complexity of it, the charges (and therefore E_{cov} and E_{coul}) depend only on the independent variables x_j (whose number is equal to the number of cations). In order to reduce the number of variables, we group cations (of the same nature and of the same formal charge) into families with similar steric environments, measured by a small difference δy_j^2, as small as we want. Lastly, the energy is minimized as function of the remaining variables x_k using a Newton-Raphson algorithm. This approach ensures extremely fast calculation of equilibrium charges.

For each pure oxide TiO_2 and SnO_2, adjustable parameters are separated into two groups: those relative to the intrinsic properties of the atoms (χ_A^0, J_{AA}^0, R_A^{eff}) and those relative to the interactions between them (A_{M-O}, p, q, ξ_0). The parameters are optimized in order to

reproduce the lattice parameters, the cohesive energy and the bulk modulus of the perfect pure oxide crystals. All the parameters are reported in TABLE 2. The calculated properties obtained with these parameters compared to the experimental ones are reported in TABLE 3.

$Intrinsec\ param$	χ_0^I (eV)	J_{II}^0 (eV)	R_I (Å)			
Ti	0.0941	10.568	0.7286			
Sn	0	10.74	0.71695			
O	6.57	10.22	0.543			
$Interaction\ param$	A_{M-O} (eV)	p	ξ_0 (eV)	q	A_{O-O} (eV)	ρ
Ti-O	0.1736	11.371	0.3598	2.291		
Sn-O	0.1645	10.705	0.2511	2.7086		
O-O					580.44	0.354

TABLE 2: SMTB-QB model parameters for rutile TiO_2 and SnO_2.

	TiO_2		SnO_2	
Parameter	SMTB-QB	Experimental	SMTB-QB	Experimental
$\|Q_O\|$	1.224		1.516	
a (Å)	4.597	4.594[a]	4.7389	4.74[d]
c (Å)	2.9594	2.959[a]	3.191	3.19[d]
u	0.3035	0.305[a]	0.307	0.307[d]
B (GPa)	211	211[c]	205	205, 208
E_{coh}(eV)	-19.8978	-19.9[b]	-15.5099	-15.5[e]

TABLE 3: Comparison between experimental and calculated crystal properties for rutile TiO_2 and SnO_2. Experimental values correspond to references : [a] [46], [b] [54], [c] [55], [d] [47,48] , [e] value cited in [56]. $|Q_O|$ is a result of calculations.

First, we calculate $\Delta H^{mixing}(c)$, defined as the difference between the cohesive energy of a random solid solution (rss), $E^{rss}(c)$, and the Vegard law $\left(c\,E_{coh}^{SnO_2} + (1-c)E_{coh}^{TiO_2}\right)$, as a function of c in the mixed oxide $Sn_cTi_{1-c}O_2$ with the parameters of TABLE 2. The calculations are performed with a relaxed Monte Carlo method at 2K (this allows to equate E^{rss} and H^{rss}). For each composition c, ten rss were built to ensure accurate results. Details of the Monte Carlo simulations are reported in the APPENDIX A. Calculated $\Delta H^{mixing}(c)$ curve is shown in FIG. 2(a) and compared with the DFT data from Liu *et al,* which leads to a critical temperature

value consistent with the literature [11]. The experimental values obtained by Ma and Navrotsky [42] are highly dispersed and correspond to a fairly low critical temperature. Physical characteristics, as the parabolic shape of the curve and the positive values over the whole concentration range showing the tendency of the system towards phase separation in accordance with the experimental phase diagram (FIG. 1(b)), are well reproduced. Nevertheless, the maximum value $\Delta H^{mixing}(c = 0.5) \approx 170$ meV/mol is much greater than the DFT value (≈ 90 meV/mol) which means that the critical temperature (T_c) itself is greatly overestimated (of about a factor 2 as estimated with a simple Ising model) [57]. In order to reduce T_c, we must make E^{rss} more cohesive. We find that the best way is to act on the covalent part of the energy, E_{cov}. In fact, it seems likely that the mixture Ti/Sn on the cationic sublattice must modify the covalence with oxygen of each of the cations. Thus, we opted for the use of a unique averaged electron hopping integral $\langle \xi_{CO} \rangle_0$. The procedure to obtain this parameter is detailed in the APPENDIX A.

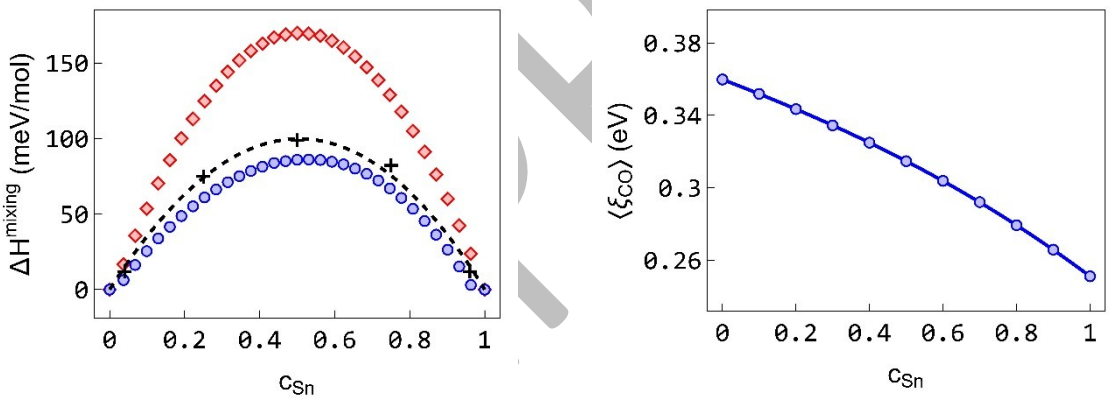

FIG. 2. (a) Mixing enthalpy $\Delta H^{mixing}(c) = E^{rss}(c) - \left(c\, E_{coh}^{SnO_2} + (1-c)E_{coh}^{TiO_2}\right)$ as a function of the nominal concentration for $Sn_cTi_{1-c}O_2$ issued from MC simulations at $T = 2$ K with parameters of TABLE 2 (red diamond), unique hopping integral $\langle \xi_{CO} \rangle_0$ (blue disk) and DFT data (black cross) [11]. (b) Evolution of the unique hopping integral $\langle \xi_{CO} \rangle_0$, as a function of the nominal concentration.

C. Effective Site Energy model

1. Hamiltonian

We consider the $\mathrm{Sn_cTi_{1-c}O_2}$ mixed oxide composed of N_{Sn} atoms Sn and N_{Ti} atoms Ti ($N_C = N_{Sn} + N_{Ti}$ and $c = N_{Sn}/N_C$). The total energy of a system of concentration c (rss, ordered structures) with periodic boundary is given by the following Hamiltonian:

$$H = \sum_{I=Sn,Ti,O} \sum_{i=1}^{N_I} E_I^{p_i}(c) \tag{9}$$

where $E_I^{p_i}(c)$ is the energy of the i-th atom I $(= Sn, Ti, O)$ and p_i is the number of Sn atoms in the nearest neighboring shell of this atom.

In a mean-field approximation (MFA), the Hamiltonian of a rss can be written as a function of the site energies using a combinatorial description [28]

$$\begin{aligned} H = N_C \sum_{p=0}^{Z} C_Z^p c^p (1-c)^{Z-p} \left(c\, E_{Sn}^p + (1-c) E_{Ti}^p \right) \\ +2N_C \sum_{p=0}^{Z_O} C_{Z_O}^p c^p (1-c)^{Z_O-p} E_O^p \end{aligned} \tag{10}$$

where Z and Z_O are respectively the number of first neighbor cations for a cation and for an oxygen atom ($Z = 10$ and $Z_O = 3$). C_Z^p (respectively $C_{Z_O}^p$) are the binomial coefficients, *i.e.* the number of ways that p Sn-neighbors can be chosen among Z (resp. Z_O) neighbors disregarding their order.

2. Computational determination of ESE

We use the SMTB-QB interatomic potentials described in section II.B to compute the site energies $E_I^p(c)$. SMTB-QB Monte Carlo calculations are performed at low temperature ($T = 2$ K) to minimize the energy of the rss. The volume of the simulation cell and the positions of atoms are optimized (details of Monte Carlo are reported in APPENDIX A).

For a given nominal concentration, Sn atoms are randomly located on the cationic sublattice. To obtain site energy values for all possible p values (between 0 and Z for cations and between 0 and Z_O for oxygen atoms), we adopt the following procedure:

- a site i is selected and its chemical nature is fixed ($I = Sn, Ti, O$);

- the local environment of the site i is constructed randomly with p nearest Sn neighbors, the remaining nearest neighbors sites are filled with Ti atoms;
- the remaining Sn atoms are randomly distributed on the cationic sublattice to attain the nominal concentration.

For cations, we consider the ten 1st neighbors with and without distinguishing by distance.

Once the configuration has been relaxed, the energy of each atom is ranked according to p, the number of Sn atoms in its nearest neighbor shell, and recorded. The total energy of the box is also recorded. The procedure is repeated for each p value and for each chemical nature I (located on site i) 10 times to reach a good statistic. The effective site energies $E_I^p(c)$ are the average values of all the energies obtained for the same local chemical environment p, at a given concentration. Total cell energy is also averaged over all configurations.

Note that the charge of each atom $Q_I^{p_i}(c)$ is also recorded and averaged according p and c.

Hereinafter, we will refer to a quantity as direct when that quantity is obtained by SMTB-QB MC simulations.

3. ESE database

ESE for $\mathrm{Sn_cTi_{1-c}O_2}$ are shown in FIG. 3 for different values of nominal rss concentration. For a given concentration, E_{Sn}^p (see FIG. 3(a)), E_{Ti}^p (FIG. 3(b)) and E_O^p (FIG. 3(c)) are almost affine. In each case there is a very slight curvature that is not well visible at this scale.

The cohesive energy of $\mathrm{TiO_2}$, $E_{coh}^{TiO_2} = -19.9$ eV/mole corresponds to $E_{Ti}^0 + 2E_O^0$ when $c \to 0$, with $E_{Ti}^0(0) = -2.3$ eV and $E_O^0(0) = -8.8$ eV. For $\mathrm{SnO_2}$, the cohesive energy $E_{coh}^{SnO_2} = -15.5$ eV/mole is recovered from $E_{Sn}^Z + 2E_O^{Zo}$ when $c \to 1$, with $E_{Sn}^Z(1) = 3.5$ eV and $E_O^{Zo}(1) = -9.5$ eV.

As expected, $E_{Ti}^0(c)$ is minimum for $c = 0$ and this rule can be extended to the other values of p : $E_{Ti}^p(c) > E_{Ti}^p(0)$. Sn's behavior is more surprising, $E_{Sn}^Z(c)$ is maximum for $c = 1$. This is also the case for any value of p : $E_{Sn}^p(c) < E_{Sn}^p(1)$. This means that a Sn atom is more cohesive in a rss than in pure oxide. For oxygen, $E_O^0(c)$ is maximum for $c = 0$ and $E_O^{Zo}(c)$ is minimum

for $c = 1$. The amplitude of variation is more than 2 times greater for cations than for oxygen, leading to $\left(E_{Ti}^{0}(c) + 2E_{O}^{0}(c)\right) > E_{coh}^{TiO_2}$ and $\left(E_{Sn}^{Z}(c) + 2E_{O}^{Zo}(c)\right) < E_{coh}^{SnO_2}$.

Let us recall that for a bimetallic alloy $\mathrm{A_cB_{1-c}}$, both elements lose energy when the concentration differs from $c = 0$ for B and $c = 1$ for A: $E_A^Z(c) > E_{coh}^A$ and $E_B^0(c) > E_{coh}^B$. This difference in behavior for the mixed oxides is important, and we'll see later the consequence on the analysis of the non-local driving force. However, even though the Sn atom is more cohesive, both SnO_2 and TiO_2 molecules in a rss are less cohesive than their respective pure oxides (see APPENDIX B).

For each concentration, the site energies shown in FIG. 3 can therefore be written, in a similar way to bimetallic alloys, as a polynomial of order 2 in p :

$$E_I^p(c) = E_I^0(c) + \frac{p}{Z_I}\left(E_I^{Z_I}(c) - E_I^0(c)\right) + \varkappa_I(c)p(Z_I - p) \qquad (11)$$

with $Z_I = Z$ for $I = Sn, Ti$ and $Z_I = Z_O$ for $I = O$. $\varkappa_I$ stands for the curvature of E_I^p. A matching with an Ising model with constant nearest-neighbor pair interactions (see APPENDIX C) shows that the linear term corresponds to pair interactions, whereas the quadratic term is an additional energy to the pairwise interactions that can be seen as a contribution from the triplets [29].

FIG. 3(d-e) shows that the charge of a cation does not depend on the local environment, only on global concentration, whereas the charge of an O atom depends on both p and c (FIG. 3(f)). We show in APPENDIX B that the charge of the system is indeed zero across the entire concentration range. However, since charges are included in the calculation of energies (Eqs. (2, 3 and 7)), we may wonder whether their variations will affect the driving forces for the phase diagram.

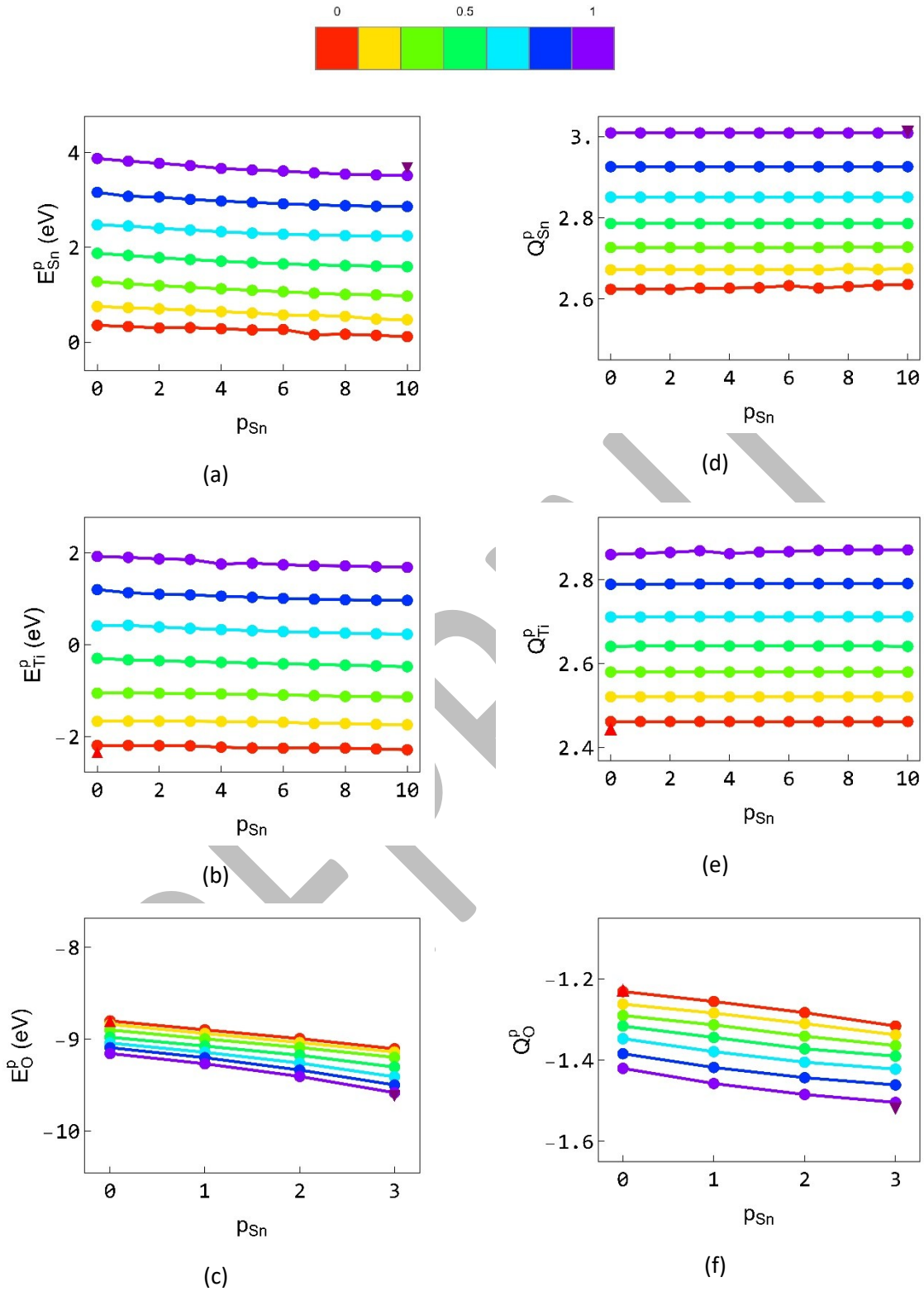

FIG. 3. Site energy (left column) and charge (right column) of an atom I as a function of the number p of Sn neighbors, for different values of the concentration in $Sn_cTi_{1-c}O_2$ oxide: I = Sn (a and d), Ti (b and e) and O (c and f). The color scales between red ($c = 0$, TiO_2-pure system) and purple ($c = 1$, SnO_2-pure system). Site energies and charge values of pure oxides are indicated with triangles, red up triangle for TiO_2 and purple down triangle for SnO_2.

D. Validation of the ESE model

To validate the ESE model, we compare the mixing enthalpy with direct calculation. The mixing enthalpy, ΔH^{mixing}, corresponds to the formation energy of a rss and its sign gives the tendency to demix ($\Delta H^{mixing} > 0$) or to order ($\Delta H^{mixing} < 0$). In the ESE model, ΔH^{mixing} is given by:

$$\Delta H^{mixing}(c) = H(c)/N_c - \left(c\, E_{coh}^{SnO_2} + (1-c) E_{coh}^{TiO_2}\right). \quad (12)$$

Direct values are calcutated from the average internal energy of rss using SMTB-QB MC simulations. There is perfect agreement between the direct calculations and the ESE model (FIG. 4). The Hamiltonian written as a function of site energies describes accurately the system. This validates the use of the site energies $E_I^p(c)$ and the restriction to the nearest-neighbor shell for their dependency on the local environment. The perfect agreement between the direct calculation and the ESE model (difference less than 10^{-4} eV/mol) justifies not considering the two types of cation-cation first neighbors (with short or long distances). In the case of an ordering system, it may be necessary to consider the different types of first neighbors in order to account for anisotropic ordering effects. Systems with a tendency to phase separation are much less complex and do not require such refinement.

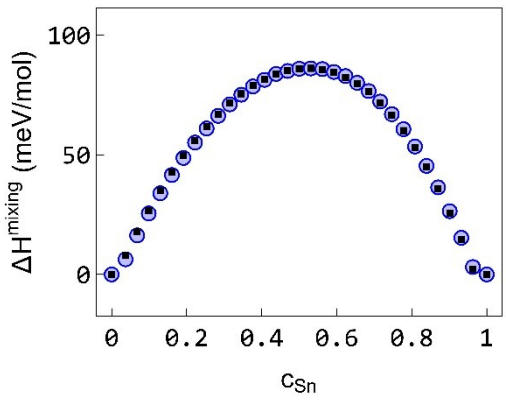

FIG. 4. Comparison of the mixing enthalpy $\Delta H^{mixing}(c)$ issued from SMTB-QB MC simulations (blue disks) and ESE model (Eqs. 12) (black squares).

The mixing enthalpy curve has a parabolic shape and the maximum value is $\Delta H^{mixing}(c = 0.5) \approx 86$ meV/mol , in agreement with DFT curve (see FIG. 2(a)).

FIG. 4 shows the evolution of the mixing enthalpy as a function of the concentration. The enthalpy of mixing is positive over the whole concentration range which means that it is more

favourable to form two pure oxide phases than a rss. The system therefore tends towards phase separation in accordance with the experimental phase diagram.

Although there may have been doubts about the applicability of a model describing local interactions to long-range interaction systems, the agreement between the direct calculation and the model justifies the use of the latter. This highlights the force of this model.

III. ESE mean-field approximation

A. Formalism

In the pseudo-grand canonical ensemble free energy F of rss is $F = H - TS - c\,N_c\Delta\mu$, with T the temperature, $\Delta\mu$ the chemical potential difference between Sn and Ti and S the configurational entropy which is written in the mean-field approximation [58]:

$$S = -k_B N_c\big(c\,\ln c + (1-c)\ln(1-c)\big) \tag{13}$$

where k_B is the Boltzmann constant.

Minimization of the free energy $\partial F/\partial c = 0$ leads to the isotherm equation:

$$\frac{c}{1-c} = exp\left(-\frac{\Delta H^{perm}-\Delta\mu}{k_B T}\right). \tag{14}$$

The permutation enthalpy ΔH^{perm} is thus the quantity that governs the chemical equilibrium [57]. This is the enthalpy variation of the system linked to the permutation of a Ti atom into an Sn atom. It is given by the derivation of the Hamiltonian (Eq. (10)) with respect to c as follows:

$$\Delta H^{perm}(c) = \frac{1}{N_c}\frac{\partial H(c)}{\partial c}. \tag{15}$$

The isotherms of an Ising model are presented in APPENDIX D. Below, we develop the formalism of the ESE model without considering triplet interactions (the curvature terms of the site energies). The complete formalism is presented in APPENDIX E.

The Hamiltonian can be expressed by combining Eqs. (10) and (11) as following:

$$\frac{\langle H\rangle}{N_c} = E^{TiO_2}(c) + c\,Z\tilde{\tau}(c) - c(1-c)\,\sum_R Z_R\tilde{V}_R(c) \tag{16}$$

where

$$Z\tilde{\tau}(c) = E^{SnO_2}(c) - E^{TiO_2}(c), \tag{17}$$

$$E^{SnO_2}(c) = E^Z_{Sn}(c) + 2E^{Z_O}_O(c) \text{ and } E^{TiO_2}(c) = E^0_{Ti}(c) + 2E^0_O(c)\,;$$

and

$$\sum_R Z_R \tilde{V}_R(c) = \left(\left(E^Z_{Sn}(c) - E^0_{Sn}(c)\right) - \left(E^Z_{Ti}(c) - E^0_{Ti}(c)\right)\right) \quad (18)$$

Note the similarities between Eq. (16) and the expression of an Ising Hamiltonian $\langle H\rangle/N_c = Z\frac{V_{BB}}{2} + c\,Z\tau - c(1-c)\,ZV$ for a system A_cB_{1-c} (see APPENDIX D). In the Ising model, τ is proportional to the difference in the cohesive energies between the two cations, A and B, and V represents the effective alloy pair interactions (EPIs). When the Ising model is restricted to nearest interactions, $\tau = (V_{AA} - V_{BB})/2$, and $V = V_1 = (V_{AA} + V_{BB} - 2V_{AB})/2$ (see APPENDIX C). When the curvatures are neglected, the Ising model is recovered when site energies do not depend on the concentration. Futhermore, matching with the Ising model, shows that $\sum_R Z_R \tilde{V}_R(c)$ corresponds to pairwise interactions.

In the ESE model, $Z\tilde{\tau}(c)$ can be understood as the energy difference between one mole of SnO_2 with the Sn atom surrounded by Z atoms of Sn, $E^{SnO_2}(c)$, and one mole of TiO_2 with the Ti atom surrounded by Z atoms of Ti, $E^{TiO_2}(c)$, each embedded in a relaxed rss of composition c.

In Eq. (16), $\sum_R Z_R \tilde{V}_R(c)$ is the term which characterizes the chemical interactions between cations in the system in a rss. Eq. (18) is obtained globally without detailing the individual $\tilde{V}_R$. In the complete formalism (see APPENDIX E), $\sum_R Z_R \tilde{V}_R(c)$ contains an additional term, which depends on the curvatures of the site energies, and which is specific to the site energy model. The question arises to whether $\sum_R Z_R \tilde{V}_R(c)$ corresponds to EPIs. This is the subject of APPENDIX F.

B. Decomposition of driving forces

1. Permutation enthalpy

The permutation enthalpy which is the central quantity of the isotherm (Eq. (14)), is deduced from Eqs. (15) and (16). The derivation of $\sum_R Z_R \tilde{V}_R(c)$ in Eq. (16) is detailed in APPENDIX E. The permutation enthalpy can be written as the sum of two contributions:

$$\Delta H^{perm} = \Delta H^{perm}_{local} + \Delta H^{perm}_{non-local}, \tag{19}$$

with

$$\Delta H^{perm}_{local}(c) = -(1-2c)\sum_R Z_R \tilde{V}_R(c) \tag{20}$$

and

$$\Delta H^{perm}_{non-local}(c) = \Delta H^{perm}_{coh}(c) + \Delta E_{\Delta c}(c), \tag{21}$$

where

$$\Delta H^{perm}_{coh}(c) = Z\tilde{\tau}(c), \tag{22a}$$

and

$$\Delta E_{\Delta c}(c) = Z\frac{\partial \tilde{\tau}(c)}{\partial c}c + \frac{\partial E^{TiO_2}(c)}{\partial c} - c(1-c)\frac{\partial \sum_R Z_R \tilde{V}_b(c)}{\partial c}, \tag{22b}$$

where $\frac{\partial \sum_R Z_R \tilde{V}_b(c)}{\partial c}$ designs the derivate of the site energies in $\sum_R Z_R \tilde{V}_R(c)$:

$$\frac{\partial \sum_R Z_R \tilde{V}_b(c)}{\partial c} = \frac{\partial}{\partial c}\left(\left(E^Z_{Sn}(c) - E^0_{Sn}(c)\right) - \left(E^Z_{Ti}(c) - E^0_{Ti}(c)\right)\right). \tag{22c}$$

For a classical Ising model (see Eq. (D3)), the permutation enthalpy contains only two contributions, the cohesive and the chemical contributions. The chemical contribution depends on the EPIs which do not vary with the concentration. Remember that EPIs govern local order, which is why this is a local contribution. When the site energies do not depend on c (and the curvatures are zero), we find that ΔH^{perm}_{local} has the same expression as ΔH^{perm}_{chem} in the Ising model and that $\Delta H^{perm}_{non-local}$ cancels out.

The non-local contribution is related to the variation in energies with nominal concentration; unlike the local contribution, it does not lead to a local order. For bimetallic alloys, the dependence on nominal concentration can be explained by elastic effects. In the present case, it could be more complex. The charge of the atoms is involved in Eqs. (3) and (7-8), so the concentration dependence could also contain electronic effects and not be due solely to elastic effect.

2. Mixing enthalpy

In the same way, it is possible to write the enthalpy of mixing from Eqs. (12) and (16) as the sum of two terms:

$$\Delta H^{mixing}(c) = \Delta H^{mixing}_{local} + \Delta H^{mixing}_{non-local}, \tag{23}$$

with

$$\Delta H_{local}^{mixing} = -c(1-c)\sum_R Z_R \tilde{V}_R(c) \quad (24)$$

and

$$\Delta H_{non-local}^{mixing} = c\left(E^{SnO_2}(c) - E_{coh}^{SnO_2}\right) + (1-c)\left(E^{TiO_2}(c) - E_{coh}^{TiO_2}\right). \quad (25)$$

The local contribution has a similar expression in the ESE and the Ising models, but in the Ising model, ΔH^{mixing} is linked to the EPIs that characterize the homoatomic or heteroatomic tendency. What's more, EPIs are not concentration-dependent.

The site energy model predicts a non-local effect (Eq. (25)) that is not contained in the Ising model. The differences $\left(E^{SnO_2}(c) - E_{coh}^{SnO_2}\right)$ and $\left(E^{TiO_2}(c) - E_{coh}^{TiO_2}\right)$ quantify energy variation of a SnO_2 and TiO_2 molecule for a nominal concentration change, which is why the second contribution is considered as non-local.

C. Driving forces

As shown in FIG. 4, the enthalpy of mixing is positive over the entire concentration range. So, the system has a tendency towards phase separation. The local and non-local effects are strongly asymmetrical (see FIG. 5). The local contribution is greatest at low concentrations, peaking at $c \approx 0.29$ ($\Delta H^{mixing} \approx 57$ meV/mol) and almost nil above $c \approx 0.65$. The non-local contribution is preponderant at high concentrations, with a maximum equal to 81 meV/mol for $c = 0.65$. Between 0 and 0.2 the non-local contribution is very small but not zero. For concentrations below 0.45, the local contribution dominates, while for $c > 0.45$ it is the non-local effect (see FIG. 5). The local contribution is mainly due to the Ising contribution, *i.e*. the term given by Eq. (18). The contribution of triplets (the second term (see Eq. (E3)) which depends of the curvatures of ESE) is less important (this contribution is not displayed on the figure).

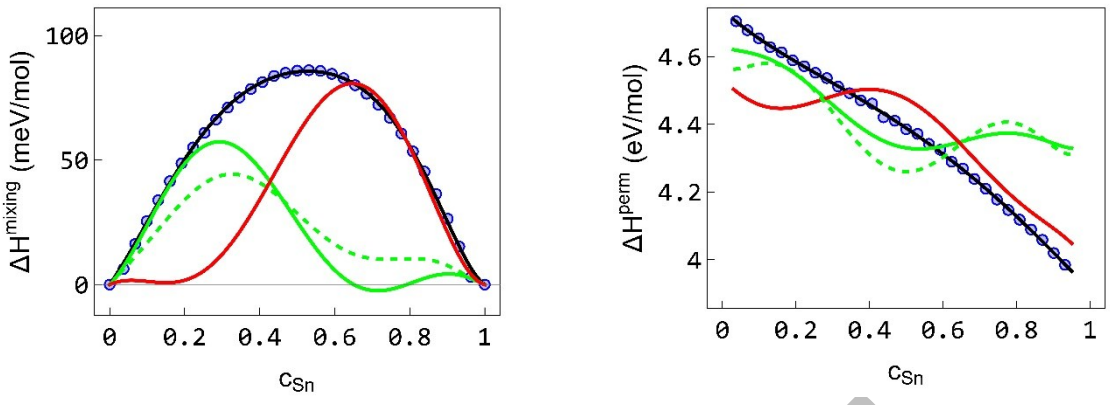

(a) (b)

FIG. 5. (a) Evolution as a function of c of the mixing enthalpy $\Delta H^{mixing}(c)$ and of its two contributions $\Delta H^{mixing}_{non-local}$ (red line) and $\Delta H^{mixing}_{local}$ (green line). (b) Evolution as a function of c of the permutation enthalpy $\Delta H^{perm}(c)$ and of its two contributions $\Delta H^{perm}_{non-local}(c)$ (red line) and $\Delta H^{perm}_{local}(c)$ (green line). In (b), $\Delta E_{coh} = E^{SnO_2}_{coh} - E^{TiO_2}_{coh}$ has been added to $\Delta H^{perm}_{local}(c)$ for better visualization. The chemical contribution of the pairs is plotted on a dashed green line ((a) and (b)). Direct SMTB-QB MC calculations are recalled with blue disks and ESE model (Eqs. (12) and (15)) (black line).

The permutation enthalpy, shown in FiG. 5(b), is almost a monotonous function as for an Ising Hamiltonian (see APPENDIX C). Remember that ΔH^{perm} and ΔH^{mixing} are linked by the relation $\Delta H^{perm} = \frac{\partial \Delta H^{mixing}}{\partial c} + \Delta E_{coh}$ with $\Delta E_{coh} = E^{SnO_2}_{coh} - E^{TiO_2}_{coh}$. The negative slope of ΔH^{perm} and the positive value of ΔH^{mixing} are consistent. For low concentrations, the slope of ΔH^{perm}_{local} is almost the same as that of ΔH^{perm}, the slope of $\Delta H^{perm}_{non-local}$ being almost zero (see FIG. 5(b)). For high concentrations it is the slope of $\Delta H^{perm}_{non-local}$ that is almost equal to the slope of ΔH^{perm} (see FIG. 5(b)).

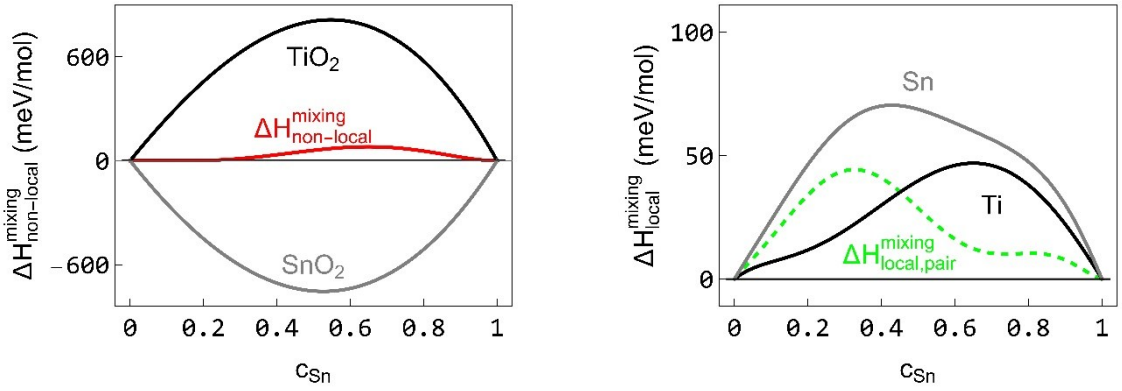

(a) (b)

FIG. 6. Evolution of $\Delta H^{mixing}_{non-local}$ (red line) (a) and pair contribution of $\Delta H^{mixing}_{local}$ (dashed green line) (b) as a function of the nominal concentration. Contributions of TiO_2 and of SnO_2 (in a) and of Ti and Sn (in b) are visualized with black and gray lines respectively.

The non-local contribution to the mixing enthalpy (Eq. (25)) is the sum of two terms, one relating to SnO_2, $\Delta H^{mixing}_{non-local,SnO_2} = c\left(E^{SnO_2}(c) - E^{SnO_2}_{coh}\right)$, and the other to TiO_2, $\Delta H^{mixing}_{non-local,TiO_2} = (1-c)\left(E^{TiO_2}(c) - E^{TiO_2}_{coh}\right)$. The non-local TiO_2 and SnO_2 contributions are opposite over the whole concentration range (FiG. 6(a)), with TiO_2's contribution being positive and SnO_2's negative. The TiO_2 contribution prevails at higher concentrations.

The sign of SnO_2's contribution is astonishing compared with bimetallic alloys. Indeed, for metals, both terms are positive, as expected for an elastic effect: in a rss of concentration c one atom surrounded by Z atoms of the same chemical nature loses energy compared to this same atom on the bulk. The negative sign of SnO_2's non-local contribution shows that the non-local effect is not only elastic, but must also contain an electronic component. In Appendix G, we present another description of the mixing enthalpy (electrostatic, repulsive and covalent). This description does not allow the electronic effects to be separated from the elastic effects. An elasticity calculation would allow this separation, but such calculations in a rss are complex and beyond the scope of this study.

For the local effect (FIG. 6(b)), as the curvatures are very small, we analyze only the contribution of pairwise interactions $\Delta H^{mixing}_{local,pair}$ which is $\Delta H^{mixing}_{local,pair} = \Delta H^{mixing}_{local,pair-Sn} - \Delta H^{mixing}_{local,pair-Ti}$. From Eqs. (12) and (18) each contribution can be written as $\Delta H^{mixing}_{local,pair-I} = -c(1-c)\left(E^Z_I(c) - E^0_I(c)\right)$. The sign of the contribution is the opposite of the sign of the slope of the site energies (see APPENDIX C). The contributions of Sn and Ti are positive whatever the value of c. As the contribution of Sn is greater than that of Ti, it drives the local effect.

To sum up, the ESE-MFA is used to extract local and non-local effects. We show that local effect predominates at low concentrations, while the non-local effect prevails at high concentrations. The phase diagram being driven by the slope of ΔH^{perm}, the decomposition of the driving forces allows one to predict that for low (respectively high) concentrations the slope of ΔH^{perm} is dominated by the slope of ΔH^{perm}_{local} (resp. $\Delta H^{perm}_{non-local}$). Since the short-range order (SRO) is driven by the EPIs and thus by ΔH^{perm}_{local}, we can expect the SRO parameter to be successively strong and then weak as the concentration increases.

D. Isotherms and phase diagram

At high temperatures, isotherms are monotonous (see FIG. 7(a)). As temperature decreases, the slope at $c = 0.5$ of the isotherm increases, until an infinite slope is reached at the critical temperature $T_c = 2200$ K. At lower temperatures, isotherms are non-monotonic with a van-der-Waals loop (see FIG. 7(a)). The S-shape of the isotherms is the signature of phase separation.

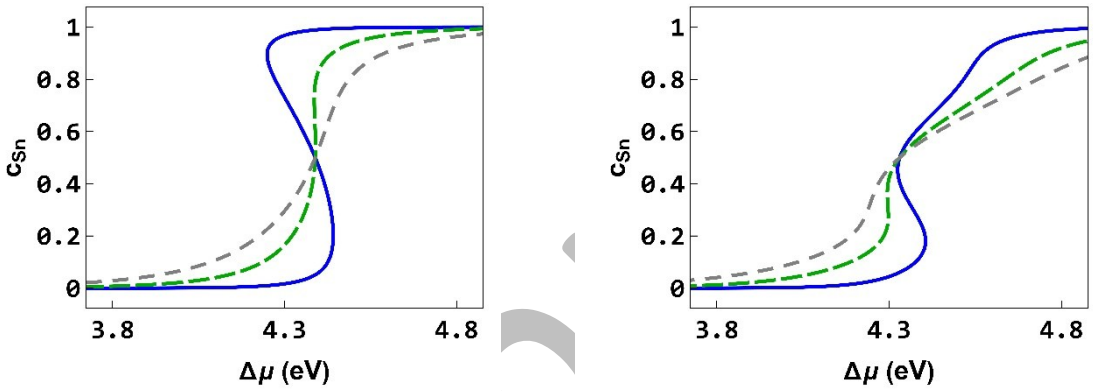

(a) (b)

FIG. 7. ESE-MFA isotherms (a) and local contribution of ESE-MFA isotherms (b) at T = 1200 K (blue line), T = 2200 K (green long dashed line), T = 3000 K (gray medium dashed line).

Since ΔH^{perm} is the key quantity governing isotherms (via Eq. (14)) and is the sum of two terms (Eq. (19)), it is possible to consider only the local contribution ΔH^{perm}_{local} to obtain the chemical contribution of ESE-MFA isotherms (see FIG. 7(b)). The local-isotherms at $T = 1200$ K and at $T = 2200$ K have an asymmetrical S-shape at low concentrations (FIG. 7(b)), when the local contribution is greatest (see FIG. 5). At high concentrations, the local-isotherm looks like a high-temperature isotherm. The critical temperature of the local contribution is therefore higher than the critical temperature of the complete system.

The phase diagram is obtained from isotherms. At each temperature, below the critical temperature T_c, in the S-shape domain, the system presents three compositions for a given chemical potential difference value. The rule of equal area is used to obtain the critical chemical potential difference $\Delta\mu_c$ and the solubility limits c_α and c_β, leading to the determination of the bulk phase diagram (see FIG. 8). The ESE-MFA phase diagram is almost identical to the equivalent Ising-MFA phase diagram (see APPENDIX D). The ESE-MFA phase diagram is symmetrical as those of the literature (see FIG. 1(b)).

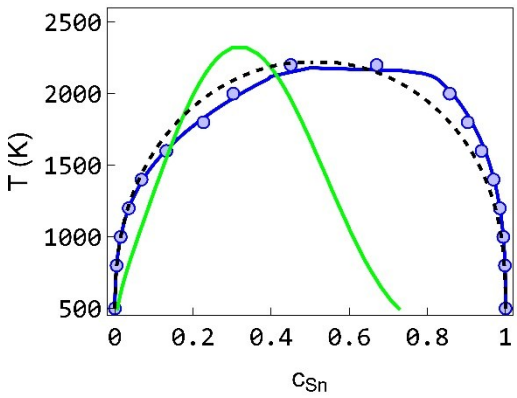

FIG. 8. Comparison of the phase diagrams issued from ESE-MFA (blue line), Ising-MFA (black dashed line), local ESE-MFA (green) and ESE-MC (blue disks).

The local phase diagram shows a miscibility gap inside the complete phase diagram. It is slightly asymmetrical and has a critical temperature value around 2360 K for $c = 0.3$. A careful examination of Figure 5(b) shows that for concentrations close to 0.3, the slope of the local contribution of the enthalpy of permutation is more negative than that of the enthalpy of permutation. This explains why the critical temperature of the local contribution is higher than that of the complete system. The non-local contribution is responsible for the difference observed between the complete phase diagram and the local phase diagram, meaning that in the region bounded by the two-phase diagram, the transition is governed by the non-local effect.

IV. ESE Monte Carlo simulations

To go beyond the MFA approximation, we also perform rigid lattice MC simulations in the canonical ensemble using the site energies. ESE-MC simulations has the advantage of being faster than off-lattice SMTB-QB MC simulations, while taking into account the effects of atomic relaxations and the influence of local composition and nominal concentration.

In the canonical ensemble, the nominal concentration c and the temperature T are fixed. A series of atomic configurations are generated by exchanging the positions of two randomly chosen atoms Sn and Ti according to a Metropolis algorithm [59]. The swap between the two atoms is accepted with probability $P = min[1, \exp(-\Delta E/k_B\, T)]$, where ΔE is the internal energy change between the initial and final states. One MC macrostep is to propose an

exchange to each of the minority atoms. To obtain the isotherm, the chemical potential difference $\Delta\mu$ is determined via Widom's method [60].

In the following we present the results obtained with a simulation box containing $N_C = 648$ cations (a total of 1944 atoms). Convergence of ESE-MC simulations is very fast. The thermodynamic quantities are averaged over $5\ 10^3$ MC macrosteps.

The local chemical order is characterized by the determination of the Warren-Cowley SRO parameter in the first neighboring shell:

$$\alpha = 1 - P_{Ti}(c,T)/Zc \qquad (26)$$

where $P_{Ti}(c,T)$ is the probability to have heteroatomic bonds in the first shell of a Ti atom [61].

A. Isotherms

We perform rigid lattice ESE-MC simulations in the canonical ensemble. FIG. 9 depicts the evolution of isotherms. The ESE-MC isotherms are in perfect agreement with the ESE-MFA ones (Eq. (14)) for the highest temperatures at $T = 3000$ K and at $T = 2200$ K, i.e. above and at the ESE-MFA critical temperature. One would expect a MC critical temperature lower than that predicted by the mean field [62]. This perfect agreement is linked to the non-local effect.

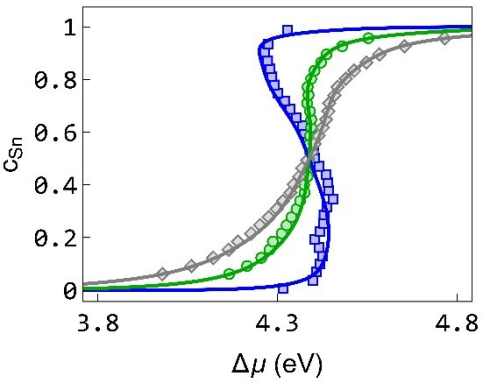

FIG. 9. Isotherms obtained from MC at T = 1200 K (blue square disk), T = 2200 K (green disk) and T = 3000 K (gray diamond). Isotherms are compared with ESE-MF (line).

At $T = 1200$ K, a temperature below the chemical critical temperature, a deviation is observed only at low concentrations when the local contribution is much greater than the non-local contribution (see FIG. 5). Around the equiatomic solution, the two contributions are of the same order of magnitude, then at higher concentrations the phase separation is driven

by the non-local effect and not by local interactions, which explains why the isotherms are identical.

Although the ESE-MC and ESE-MF isotherms differ at low temperatures for low concentrations, they are very close overall and the rule of equal areas leads to the same solubility limits and therefore to the same phase diagram (see FIG. 8).

One note that the ESE phase diagram is the incoherent phase diagram as for a real system. At a given temperature, the two coexisting phases, determined by the rule of equal areas, are at their own equilibrium parameter since the ESEs depend on the lattice parameter via the nominal concentration. The calculated phase diagram is the incoherent one while only coherent configurations are sampled.

The critical temperature is overestimated than in the literature (see FIG. 1(b)) but theoretical and experimental studies have established that the contribution of the permutation vibrational entropy can be significant [61,63,64]. Liu *et al.* have shown that taking the vibration entropy into account reduces the critical temperature by around 250 K [11], which leads to a critical temperature in good agreement with the experimental one.

B. SRO and EPIs

Even if the structures are disordered, there is a local order that can be determined using the Warren-Cowley SRO parameter α (see Eq. (26)). FIG. 10(a) shows that α is positive, the system tends to form homoatomic bonds. α is more positive the lower the temperature. SRO peaks at around $c = 0.3$ (FIG. 10(a)) and is very small for high concentrations. In the concentration range of the α peak, phase separation occurs. The very small value of α at high concentrations indicates that no phase separation occurs and ESE-MC isotherms are identical to ESE-MFA isotherms (FIG. 9).

The SRO parameter is linked to the first EPI (V_1) which is most often preponderant. So, we calculate the EPIs. Detailed calculations are presented in APPENDIX F.

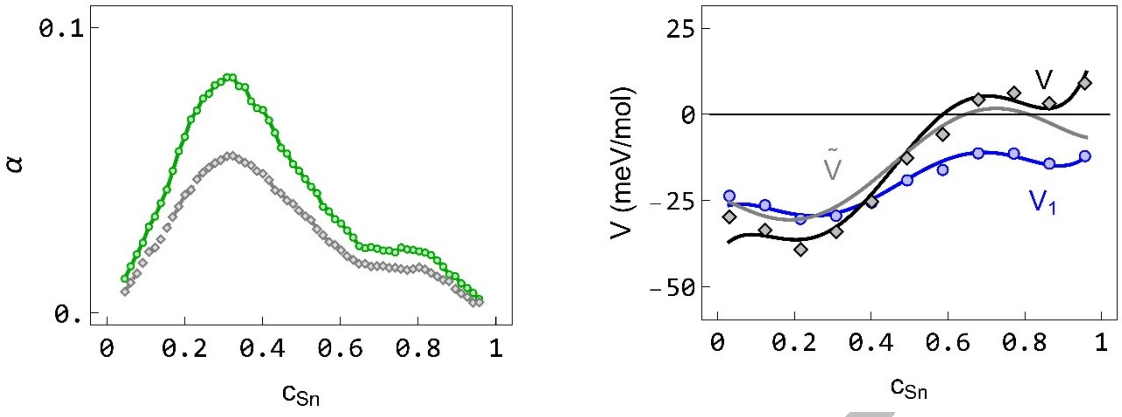

(a) (b)

FIG. 10. (a) Evolution of the SRO parameter α as a function of the concentration obtained from ESE-MC at $T = 2200$ K (green disk), $T = 3000$ K (gray diamond). (b) Evolution of $V = \left(\sum_{R=1,7} Z_R V_R\right)/Z$ (black diamonds) and of V_1 (blue disks) as a function of the nominal concentration. Comparison of the direct calculation (symbols) and ESE formalism (Eqs. (F7) and (F8)) (line). $\tilde{V} = \left(\sum_{R=1,7} Z_R \tilde{V}_R\right)/Z$ is drawn in gray.

The sign of the nearest neighbor alloy pair interaction, V_1, reflects the alloy's tendency to form homoatomic $(V_1 < 0)$ or heteroatomic pairs $(V_1 > 0)$. A perfect agreement is observed (see FIG. 10(b)) between the direct calculation (see APPENDIX F) and the analytical formula (Eq. (F7)). V_1 is negative over the entire concentration range (see FIG. 10(b)). The system tends to form homoatomic bonds, which is consistent with the local order parameter the SRO parameter α (see FIG. 10(a)).

FIG. 10(b) displays the evolution of V_1, of $V = \sum_R Z_R V_R/Z$ and of $\tilde{V} = \sum_R Z_R \tilde{V}_R/Z$ as a function of the concentration. The negative sign of $\tilde{V}$ is consistent with the positive sign of $\Delta H_{local}^{mixing}$ (see Eq. (24)). V and of $\tilde{V}$ are close. The complementary term proportional to the difference in cation curvature that appears in the expression of V (Eq. (E8)) is almost negligible. This is why the local contributions of the ESE and Ising models are very similar.

V. Conclusion

In this work, we have shown that the effective site energy model, initially developed for bimetallic alloys, can be extended to mixed oxides. The ESEs are calculated by optimization of atomic position of random solid solutions using SMTB-QB interatomic potentials. These potentials, which optimize the charges on the atoms, are used for the first time to study a

mixed oxide. The enthalpy of mixing of the system is successfully reproduced by fitting a unique electron hopping integral for both cations so as to modify the covalence with the oxygen of each of the cations.

The ESE model shows that the energies of all atoms (cations and oxygen) can be analyzed as a function both of the local environment (number of Sn nearest neighbors) and of the nominal concentration.

The perfect agreement between the direct calculation of the mixing energy via the SMTB-QB and the calculation with the ESE model demonstrates the validity of an energy model based on short-range interactions but dependent on nominal concentration. This success in long-range interaction systems such as mixed oxides is quite remarkable and allows one for its generalization beyond the $SnTiO_2$ system studied here.

Monte Carlo simulations using the ESEs reproduce quantitatively the experimental phase diagram, which shows a large and almost symmetrical miscibility gap.

Analysis of the driving forces governing the phase diagram, which is made possible by the ESE approach, reveals that the apparent symmetry of the phase diagram is in fact the result of two highly asymmetrical driving forces. The local effect that induces a homoatomic short range order dominates when Sn is the minority element, while the non-local effect that does not induce SRO dominates when Sn is the majority element.

We hope that this work will give rise to further experimental studies devoted to the determination of SRO on the whole concentration range in mixed oxides to highlight any asymmetries even if the phase diagram is symmetrical.

APPENDIX A: ADJUSTMENT OF $\langle \xi_{CO} \rangle_0$

In order to decrease the transition temperature T_c, we opted for a unique averaged value of hopping integral $\langle \xi_{CO} \rangle_0$ to determine the covalent energy of the mixed oxide. $\langle \xi_{CO} \rangle_0$ has to be viewed as the average of the hopping integral ξ_0 of the pure binary oxides TiO_2 and SnO_2 weighted by the number of hybridized orbitals n_j^0 ($= 6$ for Ti and $= 4$ for Sn). Thus, for the composition $c = 0.5$, $\langle \xi_{CO} \rangle_0 (c = 0.5) \approx \left(6 \times \xi_0^{Ti} + 4 \times \xi_0^{Ti}\right)/10 = 0.3163$.

A value $\langle \xi_{CO} \rangle_0 = 0.3147$ has been a little bit adjusted to obtain the DFT value of $\Delta H^{mixing} \approx 90$ meV/mol (FIG. 2(a)). $\langle \xi_{CO} \rangle_0$ is obviously a function of the composition c and for $c = 0$ and $c = 1$, the respective values of $\langle \xi_{CO} \rangle_0$ are equal to the value of $n_j^0 \times \xi_0$ for pure TiO_2 and pure SnO_2, as it should be. Thus, $\langle \xi_{CO} \rangle_0 (c)$ may be estimated by the relation:

$$\langle \xi_{CO} \rangle_0 (c) \approx \left((1-c) \times 6 \times \xi_0^{Ti} + c \times 4 \times \xi_0^{Ti}\right) / \left((1-c) \times 6 + c \times 4\right). \qquad \text{(A1)}$$

In order to obtain a parabolic curve for $\Delta H^{mixing}(c)$ we then adjusted two additional values of $\langle \xi_{CO} \rangle_0$ at $c = 0.25$ and $c = 0.75$. To be able to make calculations at any composition we fitted the five values of $\langle \xi_{CO} \rangle_0$ to a fourth-degree polynomial:

$$\langle \xi_{CO} \rangle_0 (c) = 0.3598 - 0.078\, c - 0.01455\, c^2 - 0.0229\, c^3 + 0.0075\, c^4 \qquad \text{(A2)}$$

The total curve $\Delta H^{mixing}(c)$ calculated with this relation is represented FIG. 2(a) as blue disks.

In all this study the Monte Carlo simulation details are as follows. Every parameter has been optimized to ensure good statistics and small errors in energy, lattice parameters and charges values. The simulation box contains 1944 atoms (648 cations and 1296 oxygens). Each run counts 1000 Monte Carlo steps by atom, 600 being retain for statistic. Both lattice parameters and atom relaxations are performed at each step, the acceptance ratio being very close to 50%. Error on cohesive energy is less than 10^{-3} eV (on about 20 eV), error on lattice parameters is less than $3\ 10^{-3}$ Å and error on charges is negligible.

APPENDIX B: ENERGY AND CHARGE

In this APPENDIX we present the evolution of the energy and of the charge as a function of concentration.

The system energy, $E = H/N_c$ with H given by Eq. (10), is the sum of two terms, $E = E_{SnO_2} + E_{TiO_2}$, which are written as:

$$E_{SnO_2}(c) = c\left(\sum_{p=0}^{Z} C_Z^p c^p (1-c)^{Z-p} E_{Sn}^p + 2\sum_{p=0}^{Z_O} C_{Z_O}^p c^p (1-c)^{Z_O-p} E_O^p\right) \quad \text{(B1)}$$

and

$$E_{TiO_2}(c) = (1-c)\left(\sum_{p=0}^{Z} C_Z^p c^p (1-c)^{Z-p} E_{Ti}^p + 2\sum_{p=0}^{Z_O} C_{Z_O}^p c^p (1-c)^{Z_O-p} E_O^p\right). \quad \text{(B2)}$$

Figure B1(a) shows that energy varies between the cohesive energy of TiO_2 (for $c = 0$) and that of SnO_2 (for $c = 1$) and that SnO_2 and TiO_2 molecules are less cohesive in a rss than in the respective pure oxides.

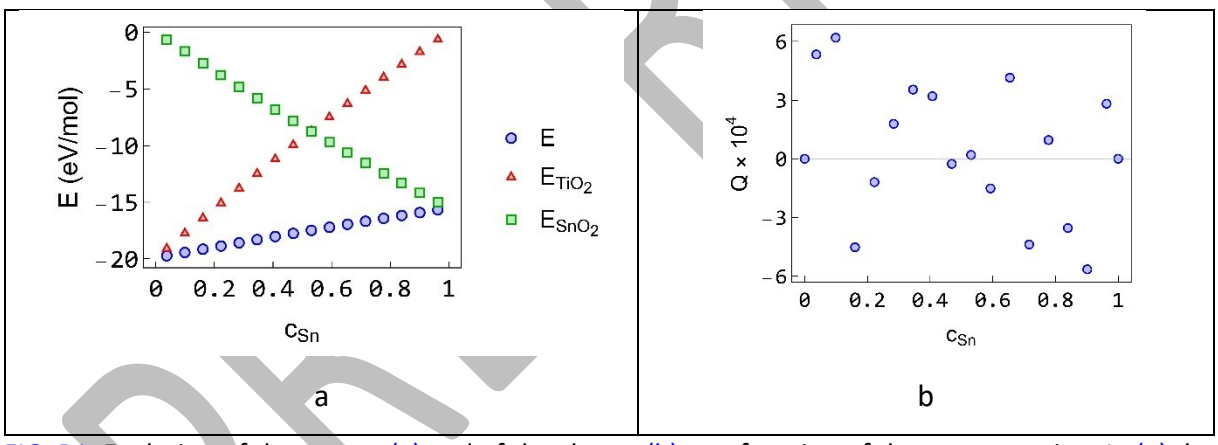

FIG. B1. Evolution of the energy (a) and of the charge (b) as a function of the concentration. In (a) the energy of the SnO_2 and the TiO_2 molecules are plotted respectively in red triangles and in green square.

The system charge is derived from the same combinatorial description as for energy as a function of site charges:

$$Q_{tot} = \sum_{p=0}^{Z} C_Z^p c^p (1-c)^{Z-p}\left(c\, Q_{Sn}^p + (1-c) Q_{Ti}^p\right) + 2\sum_{p=0}^{Z_O} C_{Z_O}^p c^p (1-c)^{Z_O-p} Q_O^p. \quad \text{(B3)}$$

As expected, the charge of the system is zero across the entire concentration range (FIG. B1(b)).

APPENDIX C: ISING MODEL

In this APPENDIX we detail the site energies for a system A_cB_{1-c}in the case of an Ising model with constant first neighbor bond energies V_{IJ} (I,J =A, B). The energy of an atom varies linearly with the number p of its nearest A neighbors, as $(pV_{AA} + (Z-p)\,V_{AB})/2$ for an atom A and as $(pV_{BA} + (Z-p)\,V_{BB}\,)/2$ for an atom B, with $V_{AB} = V_{BA}$. The energy of an atom A (respectively a B atom) varies from $E_A^0 = ZV_{AB}/2$ to $E_A^Z = ZV_{AA}/2$ (resp. from $E_B^0 = ZV_{BB}/2$ to $E_B^Z = ZV_{BA}/2$) and the slope is equal to $s_A = (V_{AA} - V_{AB})/2$ (resp. $s_B = (V_{BA} - V_{BB})/2$). The evolution of site energies A and B is schematically displayed on FIG. C1.

The Ising parameter $\tau = (V_{AA} - V_{BB})/2$ is given by $\tau = (E_A^Z - E_B^0)/Z$, and the effective nearest pair interaction $V = (V_{AA} + V_{BB} - 2V_{AB})/2$ is equal to the difference in slopes $V = (s_A - s_B)$.

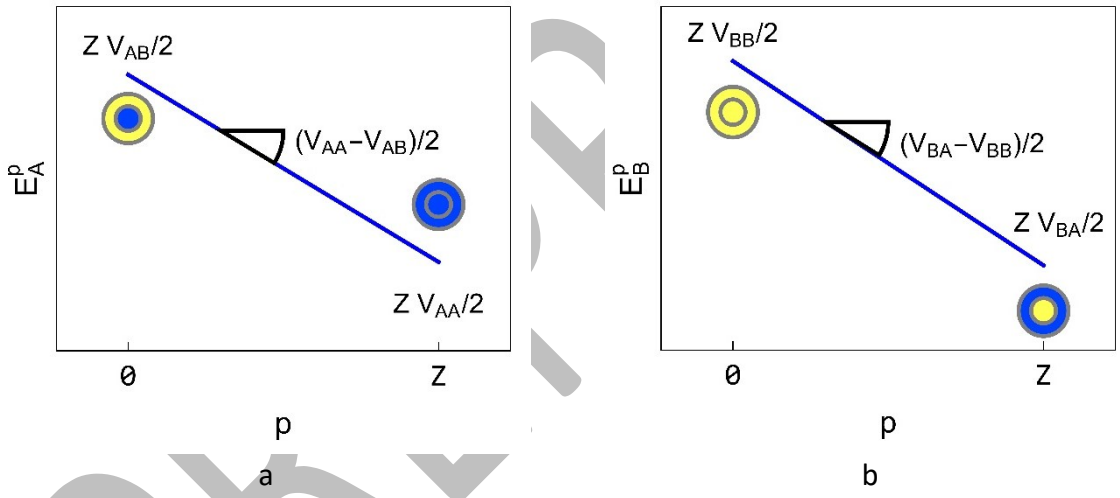

FIG. C1. Schematic evolution of site energies A (a) and B (b) of an A_cB_{1-c} alloy for an Ising model with constant nearest-neighbor bond energies. A and B atoms are shown in blue and yellow respectively. The atom in question (A or B) is represented schematically by the inner disc, and its nearest neighbors by the outer shell.

APPENDIX D: ISING ISOTHERMS

The Ising Hamiltonian is written as:

$$H = \frac{1}{2}\sum_{I,J}\sum_{n,m\neq n} p_n^I p_m^J V_{nm}^{IJ} \quad \text{(D1)}$$

with p_n^I the occupation number that equals 1 if the site n is occupied by an atom I and 0 otherwise. V_{nm}^{IJ} is the pair interaction energies between an atom I at site n and an atom J at site m.

The energy of the system can be expressed according to the Bragg Williams approximation as follows:

$$\langle H\rangle/N_{at} = \sum_R Z_R\tau_R\, c - c(1-c)\sum_R Z_R V_R + \sum_R Z_R V_R^{BB}/2 \quad \text{(D2)}$$

where R denotes the range of interactions, Z the coordination number, τ and V are defined in APPENDIX C.

The permutation enthalpy is deduced from Eq. (15) and Eq. (D2):

$$\Delta H^{perm} = \sum_R Z_R\tau_R - (1-2c)\sum_R Z_R V_R. \quad \text{(D3)}$$

Thus, for an Ising model with constant parameters, i.e. which do not depend on the nominal concentration, the enthalpy of permutation is an affine function which varies between $\sum_R Z_R(\tau_R - V_R)$ for $c = 0$ and $\sum_R Z_R(\tau_R + V_R)$ for $c = 1$ with a slope equal to $2\sum_R Z_R V_R$ (see FIG. D1(a)). The sign of $\sum_R Z_R V_R$ determines that of the slope. For a system that tends to form homoatomic bonds the slope is negative (see FIG. D1(a)). Below a critical temperature $T_c = -\frac{\sum_R Z_R V_R}{2\,k_B}$, the Ising isotherm defined by Eq. (14) exhibits a van der Waals loop (see FIG. D1(b)). By increasing the chemical potential difference, the system is successively stable (before point A), metastable (between points A and B), unstable (between points B and C), metastable (between points C and D) and stable (after point D). The rule of equal areas is used to obtain the solubility limits c_α (at point A) and c_β (at point D), leading to the determination of the bulk phase diagram.

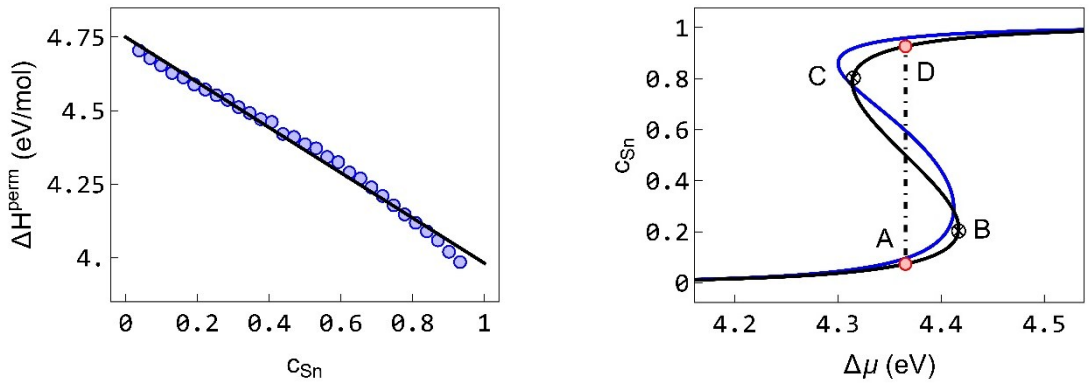

FIG. D1. Evolution of the permutation enthalpy $\Delta H^{perm}(c)$ (a) and isotherm at $T = 1500$ K (b) issued from the ESE-MFA model (Eq. (15)) (blue) and of the Ising-MFA model (black). Solubility limits are indicated with red disks (Ising-MFA). The dotted dashed vertical black line gives the Ising-MFA critical chemical potential. Points A, B, C and D indicate limits of the Ising-MFA stable, metastable and unstable states.

The evolution of the enthalpy of permutation with concentration for the ESE-MFA model is very close to that for the Ising model. Although the site energies depend on c, the curve is almost a straight line with a negative slope over the whole concentration range (see FIG. D1(a)). Consequently, the isotherms are very similar, as shown in FIG. D1(b). The solubility limits of B-rich (resp. A-rich) are very close for both models.

APPENDIX E: ESE FORMALISM

We develop in this APPENDIX the complete ESE formalism without neglecting terms that contain the curvatures. In the following, we reproduce all equations from the main text in the same order, whether modified or not, and add some calculation details.

The Hamiltonian is:

$$\frac{\langle H \rangle}{N_c} = E^{TiO_2}(c) + c\, Z\tilde{\tau}(c) - c(1-c)\, \sum_R Z_R \tilde{V}_R(c) \tag{E1}$$

with

$$\begin{gathered} Z\tilde{\tau}(c) = E^{SnO_2}(c) - E^{TiO_2}(c), \\ E^{SnO_2}(c) = E^{Z}_{Sn}(c) + 2E^{Z_O}_{O}(c) \text{ and } E^{TiO_2}(c) = E^{0}_{Ti}(c) + 2E^{0}_{O}(c)\,; \end{gathered} \tag{E2}$$

and

$$\begin{gathered} \sum_R Z_R \tilde{V}_R(c) = \Big(\big(E^{Z}_{Sn}(c) - E^{0}_{Sn}(c)\big) - \big(E^{Z}_{Ti}(c) - E^{0}_{Ti}(c)\big) \Big) \\ -Z(Z-1)\, \big(c\, \varkappa_{Sn}(c) + (1-c)\, \varkappa_{Ti}(c)\big) - 2\, Z_O(Z_O - 1)\varkappa_O(c). \end{gathered} \tag{E3}$$

As we have already mentioned in the main text, the first term corresponds to pair interactions. The correspondence with an Ising Hamiltonian has allowed us to show that the second term, which contains curvatures, is related to triplet interactions [29].

We then detail the permutation enthalpy which is obtained from the derivation of the Hamiltonian. ΔH^{perm} is obtained from Eqs. (15) and (E1). The tricky point is the derivation of $\sum_R Z_R \tilde{V}_R$ which is split into two terms:

$$\frac{\partial \sum_R Z_R \tilde{V}_R(c)}{\partial c} = \frac{\partial \sum_R Z_R \tilde{V}_a(c)}{\partial c} + \frac{\partial \sum_R Z_R \tilde{V}_b(c)}{\partial c}\,. \tag{E4}$$

$\frac{\partial \sum_R Z_R \tilde{V}_a(c)}{\partial c}$ denotes that only the combinatorial sums are differentiated:

$$\frac{\partial \sum_R Z_R\, \tilde{V}_a(c)}{\partial c} = -Z(Z-1)\, \big(\varkappa_{Sn}(c) - \varkappa_{Ti}(c)\big) \tag{E5}$$

whereas for $\frac{\partial \sum_R Z_R \tilde{V}_b(c)}{\partial c}$, only the site energies are differentiated:

$$\frac{\partial \sum_R Z_R \tilde{V}_b(c)}{\partial c} = \frac{\partial}{\partial c}\left(\left(E^Z_{Sn}(c) - E^0_{Sn}(c)\right) - \left(E^Z_{Ti}(c) - E^0_{Ti}(c)\right)\right)$$
$$- Z(Z-1)\left(c\,\frac{\partial \varkappa_{Sn}(c)}{\partial c} + (1-c)\,\frac{\partial \varkappa_{Ti}(c)}{\partial c}\right) - 2\,Z_O(Z_O-1)\frac{\partial \varkappa_O(c)}{\partial c} \quad \text{(E6)}$$

We group together all terms relating to local interactions and those relating to energy variations with the nominal composition :

$$\Delta H^{perm} = \Delta H^{perm}_{local} + \Delta H^{perm}_{non-local}. \quad \text{(E7)}$$

with

$$\Delta H^{perm}_{local}(c) = -(1-2c)\sum_R Z_R \tilde{V}_R(c) - c(1-c)\frac{\partial \sum_R Z_R \tilde{V}_a(c)}{\partial c}, \quad \text{(E8)}$$

and

$$\Delta H^{perm}_{non-local}(c) = \Delta H^{perm}_{coh}(c) + \Delta E_{\Delta c}(c), \quad \text{(E9)}$$

with

$$\Delta H^{perm}_{coh}(c) = Z\tilde{\tau}(c), \quad \text{(E10)}$$

and

$$\Delta E_{\Delta c}(c) = Z\frac{\partial \tilde{\tau}(c)}{\partial c}c + \frac{\partial E^{TiO_2}(c)}{\partial c} - c(1-c)\frac{\partial \sum_R Z_R \tilde{V}_b(c)}{\partial c}. \quad \text{(E11)}$$

We detail now the decomposition of the mixing enthalpy. Combining Eqs. (12) and (E1), we get:

$$\Delta H^{mixing}(c) = E^{TiO_2}(c) + c\,Z\tilde{\tau}(c) - c(1-c)\,\sum_R Z_R \tilde{V}_R(c) - \left(c\,E^{SnO_2}_{coh} + (1-c)E^{TiO_2}_{coh}\right) \quad \text{(E12)}$$

That can be written as:

$$H^{mixing}(c) = -c(1-c)\,\sum_R Z_R \tilde{V}_R(c) + c\left(E^{SnO_2}(c) - E^{SnO_2}_{coh}\right) - (1-c)\left(E^{TiO_2}(c) - E^{TiO_2}_{coh}\right) \quad \text{(E13)}$$

This allows us to write the enthalpy of mixing as the sum of two terms:

$$\Delta H^{mixing}(c) = \Delta H^{mixing}_{local} + \Delta H^{mixing}_{non-local}, \quad \text{(E14)}$$

with

$$\Delta H^{mixing}_{local} = -c(1-c)\sum_R Z_R \tilde{V}_R(c) \quad \text{(E15)}$$

and

$$\Delta H^{mixing}_{non-local} = c\left(E^{SnO_2}(c) - E^{SnO_2}_{coh}\right) + (1-c)\left(E^{TiO_2}(c) - E^{TiO_2}_{coh}\right). \quad \text{(E16)}$$

Eq. (E15) considers curvatures, which was not the case in the main text in Eq. (24). The local contribution is the equivalent for an Ising model to $-Z\,c(1-c)V$ which quantifies local interactions.

The differences $\left(E^{SnO_2}(c) - E_{coh}^{SnO_2}\right)$ and $\left(E^{TiO_2}(c) - E_{coh}^{TiO_2}\right)$ quantify energy variation of a SnO_2 and TiO_2 molecule for a nominal concentration change, which is why the second contribution is considered as non-local.

APPENDIX F : EFFECTIVE PAIR INTERACTION ENERGIES

We calculate in this APPENDIX the EPIs with the ESE model. EPIs are obtained from an energy balance between two configurations. The initial configuration is a rss of composition c in which two Sn atoms are located far apart. These two atoms are then repositioned on two neighboring Rth sites in the final configuration.

First, we consider the energy balance restricted to the first neighboring shell. The alloy pair interaction V_1 is the sum of three terms:

$$V_1(c) = V_{pair}(c) + n_{cn}^1\, V_{cn}(c) + n_{cn,Ox}^1\, V_{cn}^{Ox}(c) \tag{F1}$$

with $V_{pair}(c)$ the energy difference related to the two atoms of the pair itself, $V_{cn}(c)$ (respectively $V_{cn}^{Ox}(c)$) the energy difference related to the n_{cn}^1 (resp. $n_{cn,Ox}^1$) atoms, which are cationic (resp. anionic) common neighbors of the pair in the final state.

$V_{pair}(c)$ is given by:

$$V_{pair}(c) = \sum_{p=0}^{Z-1} C_{Z-1}^{p}\, c^p (1-c)^{Z-1-p} \left(\left(E_{Sn}^{p+1} - E_{Sn}^{p}\right) - \left(E_{Ti}^{p+1} - E_{Ti}^{p}\right) \right) \tag{F2}$$

The energy difference of cationic common neighbors is:

$$V_{cn}(c) = \sum_{p=0}^{Z-2} C_{Z-2}^{p}\, c^p (1-c)^{Z-2-p} \left(c\, \tilde{E}_{Sn}^{p+1} + (1-c) \tilde{E}_{Ti}^{p+1} \right), \tag{F3}$$

and that of anionic common neighbors is

$$V_{cn}^{Ox}(c) = \sum_{p=0}^{Z_O-2} C_{Z_O-2}^{p}\, c^p (1-c)^{Z_O-2-p} \tilde{E}_{Ox}^{p+1}, \tag{F4}$$

with $\tilde{E}_I^p = \left(E_I^{p+1} + E_I^{p-1} - 2E_I^p\right)/2 = \varkappa_I \; (I = Sn, Ti, O)$

The number of cationic (resp. anionic) common nearest neighbors is $n_{cn}^1 = \frac{Z_1^{SD} n_{cn}^{1,SD} + Z_1^{LD} n_{cn}^{1,LD}}{Z_1^{SD} + Z_1^{LD}}$ (resp. $n_{cn,Ox}^1 = \frac{n_{cn,Ox}^{1,SD} Z_1^{SD} + n_{cn,Ox}^{1,LD} Z_1^{LD}}{Z_1^{SD} + Z_1^{LD}}$) where Z_1^X and $n_{cn}^{1,X}$ denote coordination number and number of common neighbors at short-distance SD or long-distance LD positions. Note that $Z = Z_1 = Z_1^{SD} + Z_1^{LD}$.

In the ESE formalism, the interactions of pairs in the Rth shell of neighbors depend only on the n_{cn}^R cationic common neighbors of the pair:

$$V_{R>1}(c) = n_{cn}^R\, V_{cn}(c). \tag{F5}$$

Finally,

$$\sum_R Z_R V_R\,(c) = Z\,V_{pair}(c) + Z(Z-1)V_{cn}(c) + Z\,n^1_{cn,Ox}\,V^{Ox}_{cn}(c) \qquad \text{(F6)}$$

Values of n^R_{cn} and Z_R are given in TABLE F1. Note that $n^{R>7}_{cn} = 0$, $n^{R>1}_{cn,Ox} = 0$ and $\sum_{R=1,7} n^R_{cn} Z_R = Z(Z-1)$.

R	n^R_{cn}	Z_R	d_R	$n^R_{cn} Z_R$
1	$n^{1,SD}_{cn} = 4$	$Z^{SD}_1 = 2$	2.96	8
	$n^{1,LD}_{cn} = 2$	$Z^{LD}_1 = 8$	3.58	16
2	4	4	4.6	16
3	2	8	5.49	16
4	2	8	5.53	16
5	1	2	5.96	2
6	2	4	6.51	8
7	1	8	7.16	8
R	$n^R_{cn,Ox}$	Z_R	d_R	$n^R_{cn,Ox} Z_R$
1	$n^{1,SD}_{cn,Ox} = 2$	$Z^{SD}_1 = 2$	2.96	4
	$n^{1,LD}_{cn,Ox} = 1$	$Z^{LD}_1 = 8$	3.58	8

TABLE F1: Number of common neighbors n^R_{cn}, coordinence Z_R and distance d_R in the Rth shell of neighbors.

Given the expression of site energies as a function of p (Eq. (11)), the alloy pair interactions V_1 and $\sum_R Z_R V_R$ are written:

$$\begin{aligned} ZV_1(c) = &\left(E^Z_{Sn}(c) - E^0_{Sn}(c)\right) - \left(E^Z_{Ti}(c) - E^0_{Ti}(c)\right) \\ &+ Z(Z-1)(1-2c)\left(\varkappa_{Sn}(c) - \varkappa_{Ti}(c)\right) - n^1_{cn} Z\left(c\,\varkappa_{Sn}(c) + (1-c)\,\varkappa_{Ti}(c)\right) \\ &-2\,Z_O(Z_O-1)\varkappa_O(c), \end{aligned} \qquad \text{(F7)}$$

$$\begin{aligned} \sum_R Z_R V_R\,(c) = &\left(E^Z_{Sn}(c) - E^0_{Sn}(c)\right) - \left(E^Z_{Ti}(c) - E^0_{Ti}(c)\right) + Z(Z-1)(1-2c)\left(\varkappa_{Sn}(c) - \varkappa_{Ti}(c)\right) \\ &-Z(Z-1)\ \left(c\,\varkappa_{Sn}(c) + (1-c)\,\varkappa_{Ti}(c)\right) - 2\,Z_O(Z_O-1)\varkappa_O(c). \end{aligned} \qquad \text{(F8)}$$

Recall that EPIs give the tendency to form homoatomic or heteroatomic bonds. Eq. (F8) differs from Eq. (E3) by one additional term. This term is proportional to the difference in curvature of Sn and Ti. In fact, $Z\tilde{V}(c) = ZV(c)$ when the curvatures of Sn and Ti are zero or when they are equal $\left(\varkappa_{Sn}(c) = \varkappa_{Ti}(c)\right)$.

APPENDIX G: DECOMPOSITION OF THE MIXING ENTHALPY

The energy of the system can be expressed as the sum of four components: ionic, coulombic, repulsive and covalent, according to Eq. (1). Hereafter, we consider the electrostatic energy (the sum of the ionic and electrostatic components $E_{ELEC} = E_{ion} + E_{coul}$), the repulsive energy ($E_{REP} = E_{rep}(M-O) + E_{rep}(O-O)$) and the covalent energy to separate their contribution in the mixing enthalpy.

The figure G1 shows the evolution of these contributions to the mixing enthalpy (FIG. G1(a)) and to its SnO_2 (FIG. G1(b)) and TiO_2 (FIG. G1(c)) components.

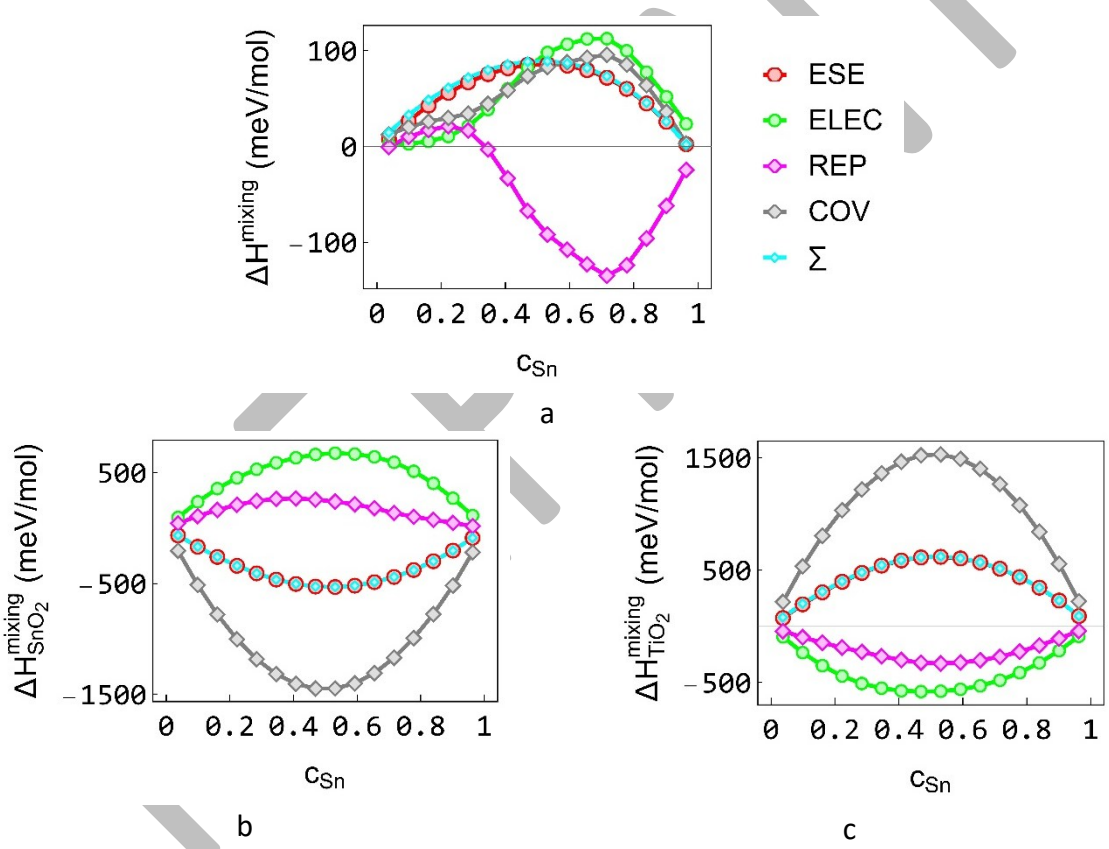

FIG. G1. Evolution of the mixing enthalpy $\Delta H^{mixing}(c)$ (a) and contributions from SnO_2 (b) and TiO_2 (c) as a function of concentration issued from the ESE formalism (red disks). The relative electrostatic ('ELEC'), repulsive ('REP') and covalent ('COV') contributions are respectively in green disks, pink diamonds and gray diamonds as indicated in (a). Small cyan diamonds correspond to the sum of these three contributions ('Σ') in order to verify consistency with ESE calculation.

The covalent part has always the same sign as the enthalpy of mixing considered (total (FIG. G1(a)) or of its SnO_2 and TiO_2 contributions (FIG. G1(b) and (c))). Without mentioning

local/non-local or elasticity, we can already note that the contributions of SnO_2 and TiO_2 are opposite, with that of TiO_2 outweighing that of SnO_2.

The decomposition of the local contribution is shown in FIG. G2(a). The repulsive and covalent terms, which are opposite, roughly cancel each other out. The electrostatic term constitutes approximately the local contribution. The local contributions of SnO_2 and TiO_2 are again opposite (FIG. G2(b) and (c)), but this time the contribution of SnO_2 prevails. The electrostatic component has the same sign as the local mixing enthalpy considered (for SnO_2 and TiO_2 components).

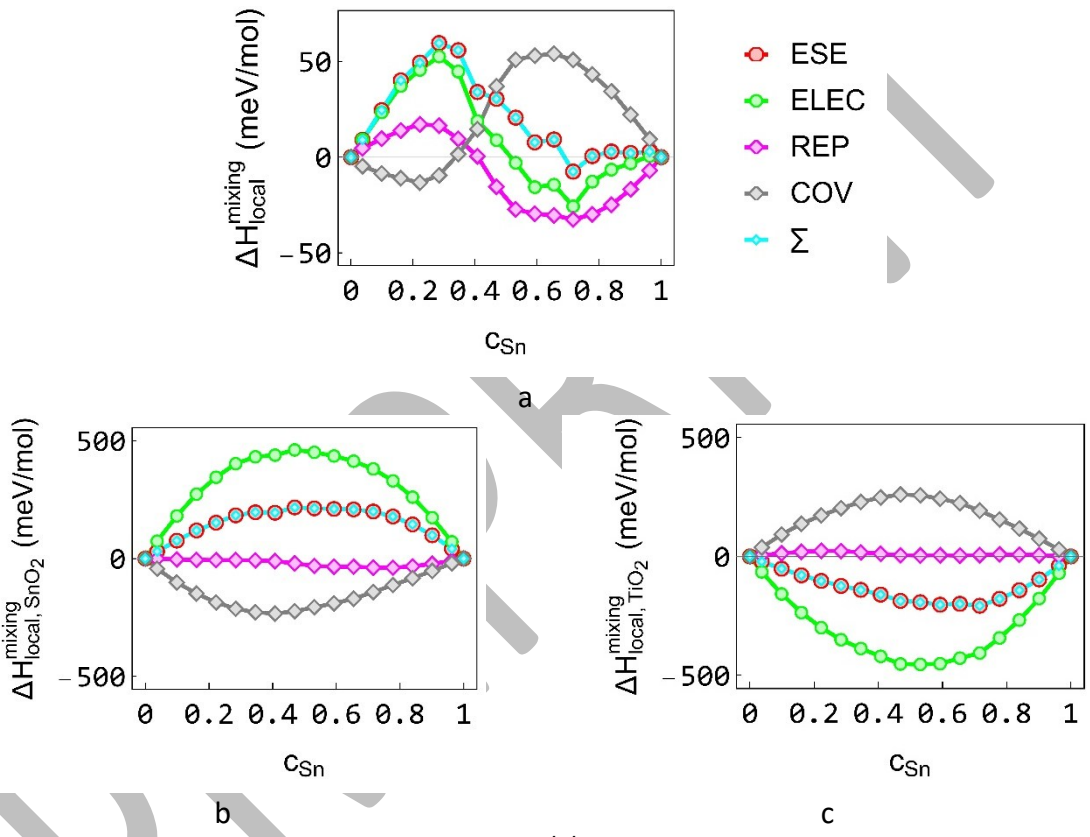

FIG. G2. Evolution of the local mixing enthalpy $\Delta H^{mixing}_{local}(c)$ (a) and contributions from SnO_2 (b) and TiO_2 (c) as a function of concentration issued from the ESE formalism (red disks). The relative electrostatic ('ELEC'), repulsive ('REP') and covalent ('COV') contributions are respectively in green disks, pink diamonds and gray diamonds as indicated in (a). Small cyan diamonds correspond to the sum of these three contributions ('Σ') in order to verify consistency with ESE calculation.

The decomposition of the non-local contribution does not show any predominant term (FIG. G3(a)). The covalent component has the same sign as the non-local mixing enthalpy considered (total (FIG. G3(a)) or of its SnO_2 and TiO_2 components (FIG. G3(b) and (c))) over the entire concentration range. As we have already seen (FIG. 5(a)), the non-local contributions of SnO_2 and TiO_2 are opposite: the contribution of TiO_2, which is positive, has the same sign as the non-local contribution, while that of SnO_2 is negative.

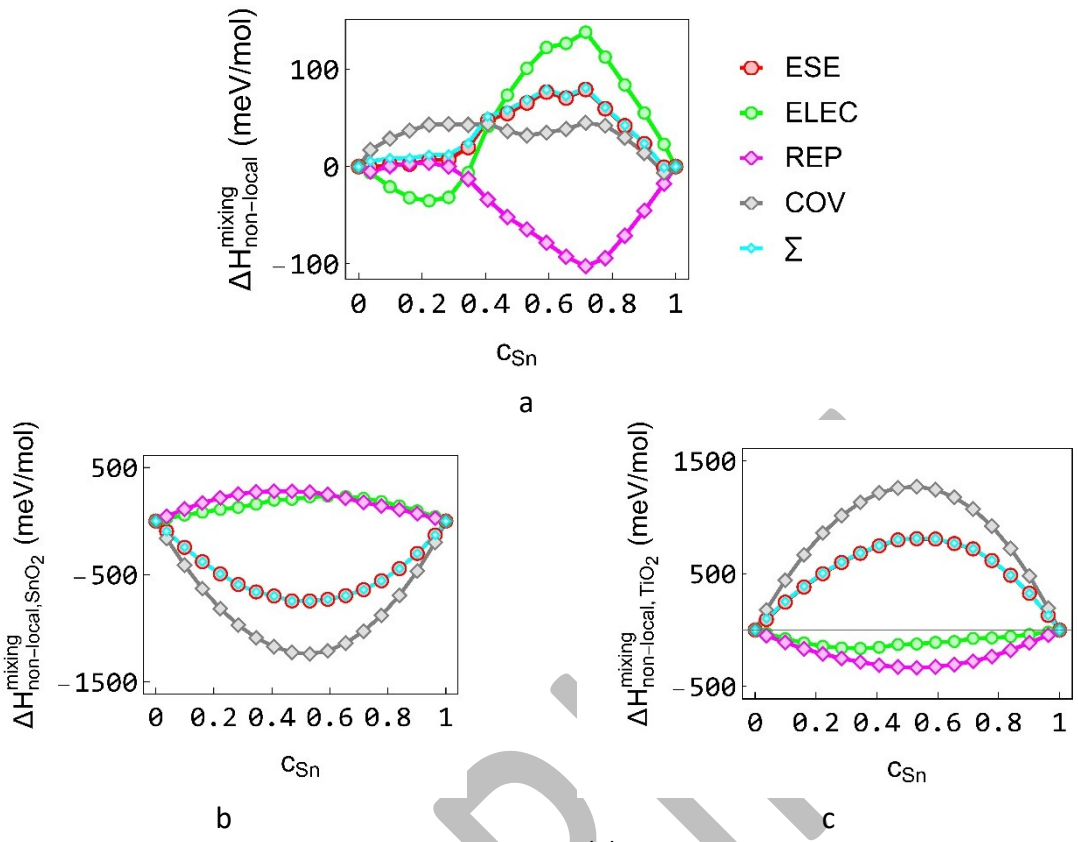

FIG. G3. Evolution of the non-local mixing enthalpy $\Delta H^{mixing}_{non-local}(c)$ (a) and contributions from SnO_2 (b) and TiO_2 (c) as a function of concentration issued from the ESE formalism (red disks). The relative electrostatic ('ELEC'), repulsive ('REP') and covalent ('COV') contributions are respectively in green disks, pink diamonds and gray diamonds as indicated in (a). Small cyan diamonds correspond to the sum of these three contributions ('Σ') in order to verify consistency with ESE calculation.

It can be seen that all the curves for the SnO_2 and TiO_2 contributions (local, non-local) are very regular, but that their sums result in irregular curves.

References

[1] H. Ji, A. Urban, D. A. Kitchaev, D. H. Kwon, N. Artrith, C. Ophus, W. Huang, Z. Cai, T. Shi, J. C. Kim, H. Kim, and G. Ceder, *Hidden Structural and Chemical Order Controls Lithium Transport in Cation-Disordered Oxides for Rechargeable Batteries*, Nat. Commun. **10**, (2019).

[2] L. Li, B. Ouyang, Z. Lun, H. Huo, D. Chen, Y. Yue, C. Ophus, W. Tong, G. Chen, G. Ceder, and C. Wang, *Atomic-Scale Probing of Short-Range Order and Its Impact on Electrochemical Properties in Cation-Disordered Oxide Cathodes*, Nat. Commun. **14**, 7448 (2023).

[3] X. Li, X. Chen, Q. Bai, Y. Mo, and Y. Zhu, *From Atomistic Modeling to Materials Design: Computation-Driven Material Development in Lithium-Ion Batteries*, Sci. China Chem. **67**, 276 (2024).

[4] V. S. Urusov, *Theory of Isomorphous Mixture* (Nauka, Moscow, 1977).

[5] V. S. Urusov, V. L. Tauson, and V. V. Akimov, *Geochemistry of a Solid*, GEOS (GEOS., Moscow, 1997).

[6] V. S. Urusov, T. G. Petrova, and N. N. Eremin, *Computer Simulation of the Properties of MgO-CaO Solid Solutions with Allowance for Short-Range Order*, Dokl. Phys. **47**, 811 (2002).

[7] S. Nambu and M. Oiji, *Coherent Phase Diagram for Spinodal Decomposition in the Tetragonal Titanium Dioxide—Tin Oxide System*, J. Am. Ceram. Soc. **74**, 1910 (1991).

[8] P. S. Ghosh and A. Arya, *Structural, Thermodynamic, Electronic and Elastic Properties of Th1-xUxO2 and Th1-xPuxO2 Mixed Oxides*, Phys. Chem. Chem. Phys. **22**, 6406 (2020).

[9] K. Klaa, S. Labidi, R. Masrour, A. Jabar, M. Labidi, A. Amara, A. Drici, E. K. Hlil, and M. Ellouze, *Structural, Electronic, Magnetic and Thermodynamic Properties of Ni1−xTixO Alloys an Ab Initio Calculation and Monte Carlo Study*, Phase Transitions **91**, 600 (2018).

[10] L. C. Shuller, R. C. Ewing, and U. Becker, *Thermodynamic Properties of ThxU1−xO2 (0 <x< 1) Based on Quantum–Mechanical Calculations and Monte-Carlo Simulations*, J. Nucl. Mater. **412**, 13 (2011).

[11] X. Liu, V. L. Vinograd, X. Lu, E. V Leonenko, N. N. Eremin, R. Wang, and B. Winkler, *Thermodynamics of Mixing in an Isostructural Solid Solution: Simulation Methodologies and Application to the Rutile-Cassiterite System*, Am. Mineral. **101**, 1197 (2016).

[12] G. Ceder, A. F. Kohan, M. K. Aydinol, P. D. Tepesch, and A. Ven, *Thermodynamics of Oxides*

with Substitutional Disorder: A Microscopic Model and Evaluation of Important Energy Contributions, J. Am. Ceram. Soc. **81**, 517 (2005).

[13] V. L. Vinograd, M. H. F. Sluiter, B. Winkler, A. Putnis, U. Hålenius, J. D. Gale, and U. Becker, *Thermodynamics of Mixing and Ordering in Pyrope — Grossular Solid Solution*, Mineral. Mag. **68**, 101 (2004).

[14] M. Y. Lavrentiev, N. L. Allan, G. D. Barrera, and J. A. Purton, *Ab Initio Calculation of Phase Diagrams of Oxides*, J. Phys. Chem. B **105**, 3594 (2001).

[15] N. L. Allan, G. D. Barrera, M. Y. Lavrentiev, I. T. Todorov, and J. A. Purton, *Ab Initio Calculation of Phase Diagrams of Ceramics and Minerals*, J. Mater. Chem. **11**, 63 (2001).

[16] N. L. Allan, G. D. Barrera, M. Y. Lavrentiev, C. L. Freeman, I. T. Todorov, and J. A. Purton, *Beyond the Point Defect Limit: Simulation Methods for Solid Solutions and Highly Disordered Systems*, Comput. Mater. Sci. **36**, 42 (2006).

[17] J. A. Purton, S. C. Parker, and N. L. Allan, *Monte Carlo Simulation and Free Energies of Mixed Oxide Nanoparticles*, Phys. Chem. Chem. Phys. **15**, 6219 (2013).

[18] C. Takoukam-Takoundjou, E. Bourasseau, and V. Lachet, *Study of Thermodynamic Properties of U1-YPuyO2 MOX Fuel Using Classical Molecular Monte Carlo Simulations*, J. Nucl. Mater. **534**, 1 (2020).

[19] J. A. Purton and N. L. Allan, *Multi-Million Atom Monte Carlo Simulation of Oxide Materials and Solid Solutions*, Comput. Mater. Sci. **103**, 244 (2015).

[20] C. E. Mohn, M. Y. Lavrentiev, N. L. Allan, E. Bakken, and S. Stølen, *Size Mismatch Effects in Oxide Solid Solutions Using Monte Carlo and Configurational Averaging*, Phys. Chem. Chem. Phys. **7**, 1127 (2005).

[21] A. Bosenick, M. T. Dove, V. Heine, and C. A. Geiger, *Scaling of Thermodynamic Mixing Properties in Garnet Solid Solutions*, Phys. Chem. Miner. **28**, 177 (2001).

[22] C. E. Mohn, M. Y. Lavrentiev, N. L. Allan, E. Bakken, and S. Stølen, *Size Mismatch Effects in Oxide Solid Solutions Using Monte Carlo and Configurational Averaging*, Phys. Chem. Chem. Phys. **7**, 1127 (2005).

[23] J. M. Sanchez and D. De Fontaine, *The Fee Ising Model in the Cluster Variation Approximation*, Phys. Rev. B **17**, 2926 (1978).

[24] J. M. Sanchez and D. De Fontaine, *Ordering in Fcc Lattices with First- and Second-Neighbor Interactions*, Phys. Rev. B **21**, 216 (1980).

[25] J. M. Sanchez and D. De Fontaine, *Ising Model Phase-Diagram Calculations in the Fcc Lattice with First- and Second-Neighbor Interactions*, Phys. Rev. B **25**, 1759 (1982).

[26] R. Kikuchi, *A Theory of Cooperative Phenomena*, Phys. Rev. **81**, 988 (1951).

[27] G. Ceder, P. D. Tepesch, G. D. Garbulsky, and A. F. Kohan, *Lattice Models and Cluster Expansions for the Prediction of Oxide Phase Diagrams and Defect Arrangements*, in *Theory and Applications of the Cluster Variation and Path Probability Methods* (Springer US, Boston, MA, 1996), pp. 187–201.

[28] F. Berthier, J. Creuze, and B. Legrand, *Effective Site-Energy Model: A Thermodynamic Approach Applied to Size-Mismatched Alloys*, Phys. Rev. B **95**, 224102 (2017).

[29] F. Berthier, J. Creuze, T. Gabard, B. Legrand, M.-C. Marinica, and C. Mottet, *Order-Disorder or Phase-Separation Transition: Analysis of the Au-Pd System by the Effective Site Energy Model*, Phys. Rev. B **99**, 014108 (2019).

[30] F. Berthier and B. Legrand, *Analysis of Au–Pd Driving Forces via the Effective Site Energy Model: LRO, Antisites and Enthalpy of Permutation*, J. Phys. Condens. Matter **32**, 354001 (2020).

[31] V. Rosato, M. Guillope, and B. Legrand, *Thermodynamical and Structural Properties of f.c.c. Transition Metals Using a Simple Tight-Binding Model*, Philos. Mag. A **59**, 321 (1989).

[32] M. Radecka, K. Zakrzewska, and M. Rekas, *SnO2-TiO2 Solid Solutions for Gas Sensors*, Sensors Actuators, B Chem. **B47**, 194 (1998).

[33] K. Zakrzewska and M. Radecka, *TiO2-SnO2 Composites and Solid Solutions for Chemical Nanosensors*, Procedia Eng. **47**, 1077 (2012).

[34] K. Zakrzewska, *Mixed Oxides as Gas Sensors*, Thin Solid Films **391**, 229 (2001).

[35] A. H. Schultz and V. S. Stubican, *Modulated Structures in the System TiO2-SnO2*, Philos. Mag. **18**, 929 (1968).

[36] F. R. Sensato, R. Custodio, E. Longo, A. Beltrán, and J. Andrés, *Electronic and Structural Properties of SnxTi1-XO2 Solid Solutions: A Periodic DFT Study*, Catal. Today **85**, 145 (2003).

[37] B. Sharma, A. Sharma, and J. ha Myung, *Highly Selective Detection of Acetone by TiO2-SnO2 Heterostructures for Environmental Biomarkers of Diabetes*, Sensors Actuators B Chem. **349**, (2021).

[38] K. Maver, I. Arčon, M. Fanetti, S. Al Jitan, G. Palmisano, M. Valant, and U. Lavrenčič Štangar, *Improved Photocatalytic Activity of SnO2-TiO2 Nanocomposite Thin Films Prepared by Low-Temperature Sol-Gel Method*, Catal. Today **397**–**399**, 540 (2022).

[39] N. N. Padurow, *Miscibility in the System Rutile-Cassiterite*, Naturwissenschaften **43**, 395 (1956).

[40] D. Garcia and D. Speidel, *Reexamination of the System TiO2 -SnO2*, J. Am. Ceram. Soc. **55**, 322 (1972).

[41] M. Park, T. E. Mitchell, and A. H. Heuer, *Subsolidus Equilibria in the TiO2 -SnO2 System*, J. Am. Ceram. Soc. **58**, 43 (1975).

[42] Y. Ma and A. Navrotsky, *Calorimetric Study of Heats of Mixing in SnxTi1−xO2 Rutile Solid Solutions*, J. Am. Ceram. Soc. **93**, 3432 (2010).

[43] R. Tétot, A. Hallil, J. Creuze, and I. Braems, *Tight-Binding Variable-Charge Model for Insulating Oxides: Application to TiO2 and ZrO2 Polymorphs*, EPL (Europhysics Lett. **83**, 40001 (2008).

[44] A. Hallil, E. Amzallag, S. Landron, and R. Tétot, *Properties of Rutile TiO2 Surfaces from a Tight-Binding Variable-Charge Model. Comparison with Ab Initio Calculations*, Surf. Sci. **605**, 738 (2011).

[45] J. Goniakowski and C. Noguera, *Electronic Structure of Clean Insulating Oxide Surfaces II. Modifications of the Iono-Covalent Bonding*, Surf. Sci. **319**, 81 (1994).

[46] S. C. Abrahams and J. L. Bernstein, *Rutile: Normal Probability Plot Analysis and Accurate Measurement of Crystal Structure*, J. Chem. Phys. **55**, 3206 (1971).

[47] J. Haines and J. M. Léger, *X-Ray Diffraction Study of the Phase Transitions and Structural Evolution of Tin Dioxide at High Pressure:FfRelationships between Structure Types and Implications for Other Rutile-Type Dioxides*, Phys. Rev. B **55**, 11144 (1997).

[48] M. Batzill and U. Diebold, *The Surface and Materials Science of Tin Oxide*, Prog. Surf. Sci. **79**, 47 (2005).

[49] E. Maras, N. Salles, R. Tétot, T. Ala-Nissila, and H. Jónsson, *Improved Tight-Binding Charge*

Transfer Model and Calculations of Energetics of a Step on the Rutile TiO2 (110) Surface, J. Phys. Chem. C **119**, 10391 (2015).

[50] A. K. Rappe and W. A. Goddard, *Charge Equilibration for Molecular Dynamics Simulations*, J. Phys. Chem. **95**, 3358 (1991).

[51] C. Noguera, A. Pojani, P. Casek, and F. Finocchi, *Electron Redistribution in Low-Dimensional Oxide Structures*, Surf. Sci. **507**–**510**, 245 (2002).

[52] T. Roubille, R. Ducher, R. Tétot, N. Salles, and Y. Pipon, *Diffusion Studies in UO2 with an Improved Tight-Binding Potential: SMTB-QB*, Acta Mater. **submitted**, (2025).

[53] C. Noguera, *Physics and Chemistry at Oxide Surfaces* (Cambridge University Press, 1996).

[54] D. R. Lide, editor , *CRC Handbook of Chemistry and Physics* (83rd, (CRC, Boca Raton, FL) Sec. 5, 2002).

[55] D. G. Isaak, J. D. Carnes, O. L. Anderson, H. Cynn, and E. Hake, *Elasticity of TiO2 Rutile to 1800 K*, Phys. Chem. Miner. **26**, 31 (1998).

[56] Y. Duan, *Electronic Properties and Stabilities of Bulk and Low-Index Surfaces of SnO in Comparison with SnO2 : A First-Principles Density Functional Approach with an Empirical Correction of van Der Waals Interactions*, Phys. Rev. B **77**, 045332 (2008).

[57] F. Ducastelle., *Order and Phase Stability in Alloys.*, (Cohesion Struct. Vol. 3). North-Holland/Elsevier Sci. Publ. Amsterdam (1991).

[58] W.L. Bragg and E.J. Williams, *The Effect of Thermal Agitation on Atomic Arrangement in Alloys*, Proc. R. Soc. London. Ser. A, Contain. Pap. a Math. Phys. Character **145**, 699 (1934).

[59] N. Metropolis, A. W. Rosenbluth, M. N. Rosenbluth, A. H. Teller, and E. Teller, *Equation of State Calculations by Fast Computing Machines*, J. Chem. Phys. **21**, 1087 (1953).

[60] B. Widom, *Potential-Distribution Theory and the Statistical Mechanics of Fluids*, J. Phys. Chem. **86**, 869 (1982).

[61] C. Wolverton, V. Ozolins, and A. Zunger, *Short-Range-Order Types in Binary Alloys: A Reflection of Coherent Phase Stability*, J. Phys. Condens. Matter **12**, 2749 (2000).

[62] M. E. Fisher, *The Theory of Equilibrium Critical Phenomena*, Reports Prog. Phys. **30**, 306 (1967).

[63] A. Walle and G. Ceder, *Automating First-Principles Phase Diagram Calculations*, J. Phase Equilibria **23**, 348 (2002).

[64] M. Asta and S. M. Foiles, *Embedded-Atom-Method Effective-Pair-Interaction Study of the Structural and Thermodynamic Properties of Cu-Ni, Cu-Ag, and Au-Ni Solid Solutions*, Phys. Rev. B - Condens. Matter Mater. Phys. **53**, 2389 (1996).